

Temperate rainforests near the South Pole during peak Cretaceous warmth

<https://doi.org/10.1038/s41586-020-2148-5>

Received: 1 October 2019

Accepted: 23 January 2020

Published online: 1 April 2020

 Check for updates

Johann P. Klages^{1✉}, Ulrich Salzmann², Torsten Bickert³, Claus-Dieter Hillenbrand⁴, Karsten Gohl¹, Gerhard Kuhn¹, Steven M. Bohaty⁵, Jürgen Titschack^{3,6}, Juliane Müller^{1,3,7}, Thomas Frederichs^{3,7}, Thorsten Bauersachs⁸, Werner Ehrmann⁹, Tina van de Flierdt¹⁰, Patric Simões Pereira^{10,14}, Robert D. Larter⁴, Gerrit Lohmann^{1,3,11}, Igor Niezgodzki^{1,12}, Gabriele Uenzelmann-Neben¹, Maximilian Zundel⁷, Cornelia Spiegel⁷, Chris Mark^{13,15}, David Chew¹³, Jane E. Francis⁴, Gernot Nehrke¹, Florian Schwarz², James A. Smith⁴, Tim Freudenthal³, Oliver Esper¹, Heiko Pälike^{3,7}, Thomas A. Ronge¹, Ricarda Dziadek¹ & the Science Team of Expedition PS104*

The mid-Cretaceous period was one of the warmest intervals of the past 140 million years^{1–5}, driven by atmospheric carbon dioxide levels of around 1,000 parts per million by volume⁶. In the near absence of proximal geological records from south of the Antarctic Circle, it is disputed whether polar ice could exist under such environmental conditions. Here we use a sedimentary sequence recovered from the West Antarctic shelf—the southernmost Cretaceous record reported so far—and show that a temperate lowland rainforest environment existed at a palaeolatitude of about 82° S during the Turonian–Santonian age (92 to 83 million years ago). This record contains an intact 3-metre-long network of in situ fossil roots embedded in a mudstone matrix containing diverse pollen and spores. A climate model simulation shows that the reconstructed temperate climate at this high latitude requires a combination of both atmospheric carbon dioxide concentrations of 1,120–1,680 parts per million by volume and a vegetated land surface without major Antarctic glaciation, highlighting the important cooling effect exerted by ice albedo under high levels of atmospheric carbon dioxide.

The Cretaceous Period (144–66 million years ago (Ma)) hosted some of the warmest intervals in Earth's history^{1–3}, particularly during the Turonian to Santonian stages (93.9–83.6 Ma)^{4,5}. At that time, atmospheric carbon dioxide (CO₂) concentrations were reconstructed to be around 1,000 parts per million by volume (ppmv; ref. ⁶), and average annual low-latitude sea surface temperatures probably reached ~35 °C (ref. ⁴), with only a minor bihemispheric temperature gradient extending polewards from palaeolatitudes between 50 and 60° N (refs. ^{7–9}). Only small to medium-sized ice sheets may have existed^{10,11} and global sea level was up to 170 m higher than at present^{11,12}.

Records documenting the Antarctic terrestrial environment during this mid-Cretaceous warmth are sparse^{5,13–17} and particularly rare south of the palaeo-Antarctic Circle^{13,14}. Such records, however, are critical to constrain state-of-the-art Late Cretaceous climate models⁵ for predicting the magnitude of atmospheric CO₂ concentrations¹⁸ and their effectiveness in inhibiting the build-up of major ice sheets¹⁹.

Here we reconstruct mid-Cretaceous terrestrial environmental conditions in West Antarctica by combining micro- and

macropalaeontological, sedimentological, inorganic and organic geochemical, mineralogical and palaeomagnetic data, as well as X-ray computed tomography (CT) imagery, obtained from drill cores recovered from a site within the Pine Island cross-shelf trough in the Amundsen Sea Embayment (ASE), West Antarctica (Fig. 1a). Site PS104_20-2 (73.57° S, 107.09° W; 946 m water depth) was drilled during RV *Polarstern* expedition PS104 in 2017 (ref. ²⁰). The Pine Island Trough extends from the modern fronts of the Pine Island and Thwaites glaciers, and was eroded into the ASE shelf during repeated advances of a West Antarctic Ice Sheet palaeo-ice stream throughout the Miocene to Pleistocene epochs^{21–23}. On the inner to middle continental shelf, glacial erosion combined with tectonic uplift²² exposed seaward-dipping sedimentary strata of postulated Cretaceous to Miocene age near the seafloor²⁴ (Fig. 1b). Widespread till cover on the shelf previously prevented sampling of these strata using conventional coring techniques²⁴. Deployment of the remotely operated seafloor drill rig MARUM-MeBo70 (ref. ²⁵) enabled drilling to 30.7 m below seafloor (mbsf) into the seabed to recover the dipping strata²⁰ (Figs. 1 and 2).

¹Alfred-Wegener-Institut Helmholtz-Zentrum für Polar- und Meeresforschung, Bremerhaven, Germany. ²Department of Geography and Environmental Sciences, Northumbria University, Newcastle upon Tyne, UK. ³MARUM—Center for Marine Environmental Sciences, University of Bremen, Bremen, Germany. ⁴British Antarctic Survey, Cambridge, UK. ⁵School of Ocean and Earth Science, University of Southampton, Southampton, UK. ⁶Marine Research Department, Senckenberg am Meer, Wilhelmshaven, Germany. ⁷Faculty of Geosciences, University of Bremen, Bremen, Germany. ⁸Institute of Geosciences, Christian-Albrechts-University, Kiel, Germany. ⁹Institute for Geophysics and Geology, University of Leipzig, Leipzig, Germany. ¹⁰Department of Earth Science and Engineering, Imperial College London, London, UK. ¹¹Environmental Physics, University of Bremen, Bremen, Germany. ¹²ING PAN—Institute of Geological Sciences, Polish Academy of Sciences, Biogeosystem Modelling Laboratory, Kraków, Poland. ¹³Department of Geology, Trinity College Dublin, Dublin, Ireland. ¹⁴Present address: Department of Marine Sciences, University of Gothenburg, Gothenburg, Sweden. ¹⁵Present address: School of Earth Sciences, University College Dublin, Dublin, Ireland. *A list of authors and their affiliations appears at the end of the paper. ✉e-mail: Johann.Klages@awi.de

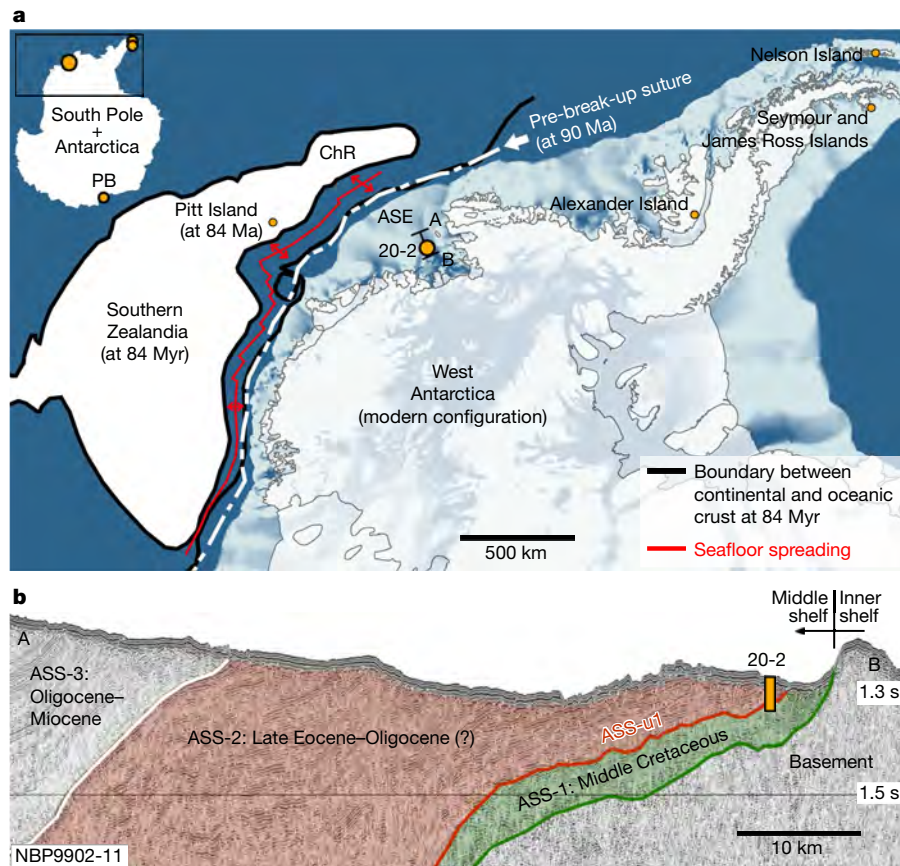


Fig. 1 | Setting of MARUM-MeBo70 drill site PS104_20-2 on the ASE shelf.

a, The present-day location of West Antarctica is shown in relation to the reconstructed boundary between continental and oceanic crust at 84 Ma (refs. ^{31,32}) (thick black lines). The pre-break up suture (dashed white line) indicates the position of the reconstructed Zealandian and West Antarctic continental and oceanic crust before initial break-up starting at -90 Ma (ref. ³¹). Orange circles mark the locations of other outcrops of mid-Cretaceous sedimentary strata¹³⁻¹⁷. **b**, Seismic reflection profile NBP9902-11²¹ (A-B)

crossing drill site PS104_20-2. The orange bar indicates the drilled core length. The profile position is indicated in **a**. The drill hole penetrated Amundsen Sea shelf unconformity ASS-u1, which separates seismic units ASS-1 and ASS-2 (ref. ²⁶). The interpretation of seismostratigraphic units and unconformities is based on both previous work²⁴ and this study. Pitt Island belongs to the Chatham Island group of New Zealand. PB, Prydz Bay; ChR, Chatham Rise. Shelf bathymetry and sub-ice topography data derive from refs. ^{54,55}.

Lithology and stratigraphy

Beneath a few metres of glacial marine and reworked glacial sediments, MARUM-MeBo70 penetrated an occasionally stratified but microfossil-barren -17–24-m-thick quartzitic gravelly sandstone with uranium–lead (U–Pb) dates on apatite and zircon grains (see Methods) constraining its maximum depositional age to -40 Myr in the late Eocene (Extended Data Fig. 1). Cores 9R and 10R recovered strata from 26.3 mbsf to the base of the hole. At -26.8 mbsf, a prominent thin (5 cm) layer of indurated lignite fragments separates the overlying sandstone unit from a ≥3-m-thick, palynomorph-rich, laminated to stratified carbonaceous mudstone below. This mudstone contains an intact and continuous network of fossil plant roots that reaches down to at least 30 mbsf (Fig. 2; Supplementary Video 1).

Based on New Zealand’s biostratigraphic ranges²⁶, the presence of the pollen taxon *Phyllocladidites mausonii* (nearest living relative (NLR): *Lagarostrobos*, Huon Pine) and the absence of both *Nothofagidites* (NLR: *Nothofagus*, Southern Beech) and *Forcipites sabulosus* within the carbonaceous mudstone indicate its deposition during the mid-Cretaceous (Turonian–Santonian; -92–83 Ma, PM1a-subzone) (Extended Data Fig. 2; Extended Data Tables 1 and 2). Abundant pollen of conifer trees (for example, *Podocarpidites*, *Trichotomosulcites*) and tree ferns (*Cyathidites*) and the presence of accessory taxa such as *Ruffordiaspora ludbrookiae* and *Tricolpites* spp. in our assemblage resemble the uppermost strata of the Turonian–Santonian Tupuangi

Formation on Pitt Island, New Zealand, dated to 92–89 Ma (refs. ^{27,28}) (Extended Data Table 3). However, the regular occurrence of pollen of the family Proteaceae, including *Beauprea*-type pollen (for example, *Peninsulapollis gillii*, *Beaupreaidites*), which are absent from the Tupuangi Formation, suggest that the ASE core is slightly younger than 89 Myr old. Recent molecular phylogenetic reconstructions indicate an early Antarctic–Southeastern Australian origin of *Beauprea* (-88 Ma), whereas the oldest palynological record of these angiosperm fossils on Antarctica and Australia date back to 81.4 Ma and 83.8 Ma, respectively²⁹.

These biostratigraphic age estimates are consistent with palaeomagnetic data obtained from discrete sediment samples showing normal polarity, expected for deposition during the ‘Cretaceous Normal Polarity Superchron’ (C34n; 121–83 Ma; ref. ³⁰) (see Methods). The layer of indurated lignite and the underlying carbonaceous mudstone show very similar pollen assemblages, which indicate a similar age and palaeoenvironment for both units (Fig. 2; Extended Data Fig. 2).

Turonian–Santonian position of the record

To assess the palaeoclimatic importance of this record, we determined the palaeogeographical position of site PS104_20-2 at 90 Ma. Today, the site is located near the Pacific continental margin of West Antarctica, about 250 km away from the modern boundary between continental and oceanic crust (Fig. 1). At the time of sediment deposition,

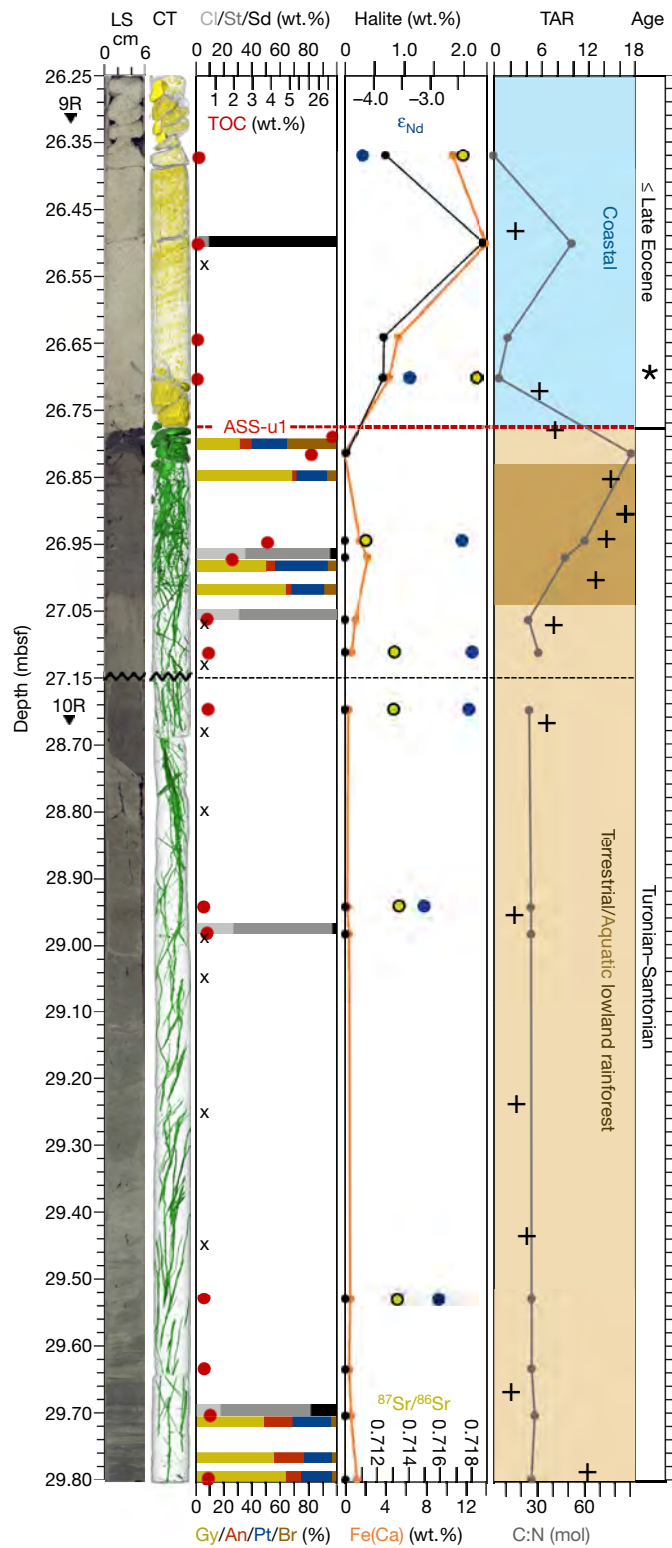


Fig. 2 | Multi-proxy parameter reconstruction of cores 9R and 10R at site PS104_20-2. The MARUM-MeBo70 seafloor drill rig drilled 30.7 m into the seafloor and recovered 5.91 m of core length. The lower -3 m consists of a fossil root-bearing mudstone with an -5-cm-thick layer of brecciated lignite on top (from -26.77 mbsf downwards), both of Turonian–Santonian age. A Late Eocene or younger quartzitic gravelly sandstone overlies the lignite. The upper lignite boundary defines the impedance contrast between the underlying mudstone and overlying gravelly sandstone and probably coincides with the prominent regional unconformity ASS-u1²⁴ (see the thick red line in Fig. 1b). Note the core break between 9R and 10R at 27.15 mbsf. LS, linescan; CT, X-ray computed tomography; Cl/St/Sd, clay/silt/sand ($n = 6$); TOC, total organic carbon ($n = 16$); Gy/An/Pt/Br, gymnosperms/angiosperms/pteridophytes/bryophytes ($n = 7$); X, barren palynomorph samples ($n = 9$); Halite ($n = 16$); Bulk sediment neodymium (ϵ_{Nd}) values (± 2 s.d. = 0.27) and strontium ($^{87}\text{Sr}/^{86}\text{Sr}$) ratios (± 2 s.e.; see Source Data) ($n = 7$) (median centre values) (see Methods); Fe(Ca), iron carbonate ($n = 16$); TAR, ratio of terrestrial and aquatic-sourced n -alkanes ($n = 14$); C:N (mol), molar ratio of TOC/TN ($n = 16$). *Zircon U–Pb age (45.5 million years (Myr)) ($n = 1$). Inferred ages are based on palynomorph biostratigraphy for the mudstone and U–Pb ages of apatite and zircon grains for the sandstone (see the main text).

wide rift zone between Zealandia and West Antarctica, just before the initiation of continental break-up^{24,31}. In a previous study³⁴, a mean palaeomagnetic pole position at 100 Ma of 75.7° S and 135.9° W with a 95% confidence radius of 3.8° for Marie Byrd Land was determined from 19 rock sample sites. By accounting for the great-circle distance of 7.84° to our drill site and rotating points on the East Antarctic polar wander path³⁴ into the Marie Byrd Land reference frame, we derive a core site palaeolatitude of 81.9° S at 90 Ma. The uncertainty in this position is estimated to be not larger than the maximum 95% confidence radius of 5.9° of the respective part of the polar wander path³⁴.

Palaeoenvironment

The indurated lignite layer as well as the laminated to stratified carbonaceous mudstone comprising the fossil plant roots in cores 10R and lower 9R at site PS104_20-2 contain a highly diverse and entirely terrestrial palynomorph assemblage of more than 62 pollen and spore taxa (Fig. 2; Extended Data Figs. 2, 3; Extended Data Table 3). The absence of palynomorphs with different stratigraphic ranges or varying thermal maturity suggests that this purely terrestrial microfossil assemblage has not been reworked. The assemblage is dominated by pollen of the conifer tree families Podocarpaceae and Araucariaceae with abundant ferns, including the tree ferns *Cyathea*, documenting the initial stages of an austral temperate rainforest (Fig. 2; Extended Data Fig. 2; Extended Data Table 2). The presence of the heterocyst glycolipids HG₃₀ triol and keto-diol (Extended Data Fig. 4; see Methods) also indicates that benthic cyanobacterial mats colonized fresh water bodies within this temperate rainforest, providing additional evidence for the development of a highly complex ecosystem in the ASE during the Turonian–Santonian. In combination with published palaeo-topographic and palaeo-tectonic information^{22,24,31,32}, the different taxa and their bioclimatic importance (see Methods) were combined and visualized to create Fig. 3. Members of the Proteaceae family presumably formed a flowering shrub understorey in the tall Late Cretaceous conifer rainforest of the ASE depicted in Fig. 3. The lignite layer is rich in spores of *Stereisporites antiquasporites* (NLR: Bryophyte, *Sphagnum*), which further suggest the temporary existence of a peat swamp in the diverse temperate lowland rainforest. This coincides with increasing *Peninsulapollis* pollen, indicating increasing humidity³⁵ towards the record's top. Thin sections were carefully prepared from resin-impregnated core samples selected from cores 9R and 10R (see Methods) to characterize the fossil roots. Although cell structures were not sufficiently preserved for identification of the plant that grew the roots, the presence of parenchyma cells within the long and continuous roots makes it likely that the network comprises

between 93 and 83 Ma, the continent of Zealandia started to rift and separate from West Antarctica^{31,32}. We applied a relative plate reconstruction between Zealandia and West Antarctica for the middle Cretaceous using the GPlates (version 2.2) plate reconstruction tool³³ with up-to-date rotation parameters of the South Pacific realm³¹. This resulted in a 736 km great-circle distance (265 km north–south distance) between the drill site and the hitherto southernmost mid-Cretaceous terrestrial palaeoenvironmental record on Pitt Island on Chatham Rise, New Zealand¹⁴. The close-fit reconstruction at 90 Ma indicates a



Fig. 3 | Reconstruction of the West Antarctic Turonian–Santonian temperate rainforest. The painting is based on palaeofloral and environmental information inferred from palynological, geochemical, sedimentological and organic biomarker data obtained from cores 9R and 10R

at site PS104_20-2. The creation of the painting was further complemented by published palaeotopographic and palaeotectonic information^{22,24,31,32}. Original size of painting: 83.8 cm × 41.5 cm. Alfred-Wegener-Institut/J. McKay; this image is available under Creative Commons licence CC-BY 4.0.

vascular plant remains and thus confirms active plant growth at our site (Extended Data Fig. 5b–e). Furthermore, the alignment of organic and clastic material within the laminated to stratified mudstone matrix (Extended Data Fig. 5a) suggests synchronous deposition of clastic particles and organic fragments.

Our environmental reconstruction is further supported by geochemical and biomarker data. In the mudstone between 29.80 and 27.03 mbsf and the indurated lignite interval (26.83–26.77 mbsf), zero to very low halite and carbonate contents in the bulk sediment fraction combined with low total organic carbon/total nitrogen (TOC/TN) ratios and low ratios of land-plant-derived long-chain *n*-alkanes versus aquatic-sourced short-chain *n*-alkanes (TAR), point to swampy aquatic freshwater conditions (Fig. 2). This interpretation is supported by the identification of cells that closely resemble aerenchyma (Extended Data Fig. 5d), which is usually responsible for intercellular gas exchange under (semi-) permanent subaquatic growing conditions³⁶. In mudstone samples taken from the core segment that contains a particularly dense root network (27.03–26.83 mbsf), pollen and biomarkers indicate the establishment of terrestrial forest-type vegetation, while elevated pristane/*n*-C₁₇ and pristane/phytane ratios point to a high abundance of terrigenous plant material (Extended Data Fig. 6; see also refs.^{37,38}), which is in line with the pollen-based interpretation of a terrestrial rainforest environment. TOC/TN ratios >20 (Fig. 2) are consistent with this interpretation and indicate a primarily land-plant source of organic matter³⁹ within this mudstone sequence.

The clay mineral assemblage in cores 9R and 10R is dominated by kaolinite (67–72%) and smectite (26–29%), both indicating chemical weathering activity under humid and (sub-) tropical climate conditions⁴⁰. However, as this is not corroborated by our reconstructed climatic setting, we attribute kaolinite formation in the mudstone to the repeated establishment of swampy conditions, in which organic acids altered silicate minerals to kaolinite ('Moorverwitterung')⁴¹.

The lithological successions in cores 9R and 10R resemble the uppermost strata of the Turonian–Santonian Tupuangi Formation on Pitt Island, New Zealand²⁷. The Pitt Island strata are characterized

by interbedded carbonaceous siltstone, quartzofeldspathic sandstone, lignite and/or peat layers. Similar to the sediment sequence described for the ASE, the Tupuangi Formation records a terrestrial, densely vegetated and partly swampy fluviodeltaic environment¹⁴. At around 90 Ma, the Tupuangi Formation was located in one of the rift basins developing before Zealandia separated from West Antarctica^{24,31}, ~736 km from Site PS104_20-2 (Fig. 1). A diverse conifer forest surrounded by extensive river systems^{42,43} seems to have covered both the Zealandian¹⁴ and the West Antarctic conjugate continental margin during this early break-up phase.

The sharp lithological change from the root-bearing fossiliferous mudstone with the thin layer of indurated lignite on top into the sandstone at 26.77 mbsf is marked by increased iron carbonate and halite contents and decreased TOC/TN and TAR ratios within the sandstone (Fig. 2), suggesting an estuarine and coastal environment. The maximum U–Pb dates of ~40 Ma obtained from the sandstone (see Extended Data Fig. 1), which is coarse-grained at its base, indicate a considerable hiatus between the mudstone (including the lignite) and the sandstone. Such a hiatus is consistent with neodymium (Nd) and strontium (Sr) isotope data, which reflect both a change in sediment provenance and a decrease in weathering intensity between the two lithologies (Fig. 2; see Methods). The time window of the hiatus coincides with slow erosion rates of a tectonically quiescent passive margin^{22,44}, whereas Eocene–Oligocene tectonic activity of the West Antarctic Rift System might have triggered renewed sedimentation of dominantly clastic material^{44,45}.

Palaeoclimate

Multi-proxy evidence from our mid-Cretaceous sedimentary record reveals an environment at a palaeolatitude of ~82° S on the Antarctic continental margin that was characterized by a regional temperate climate warm enough to maintain a diverse temperate rainforest (Fig. 3) only ~900 km from the palaeo-South Pole. Our palynomorph-based climate reconstruction following the approach outlined in ref.⁴⁶ returns a mean annual temperature of 13 °C with precipitation of

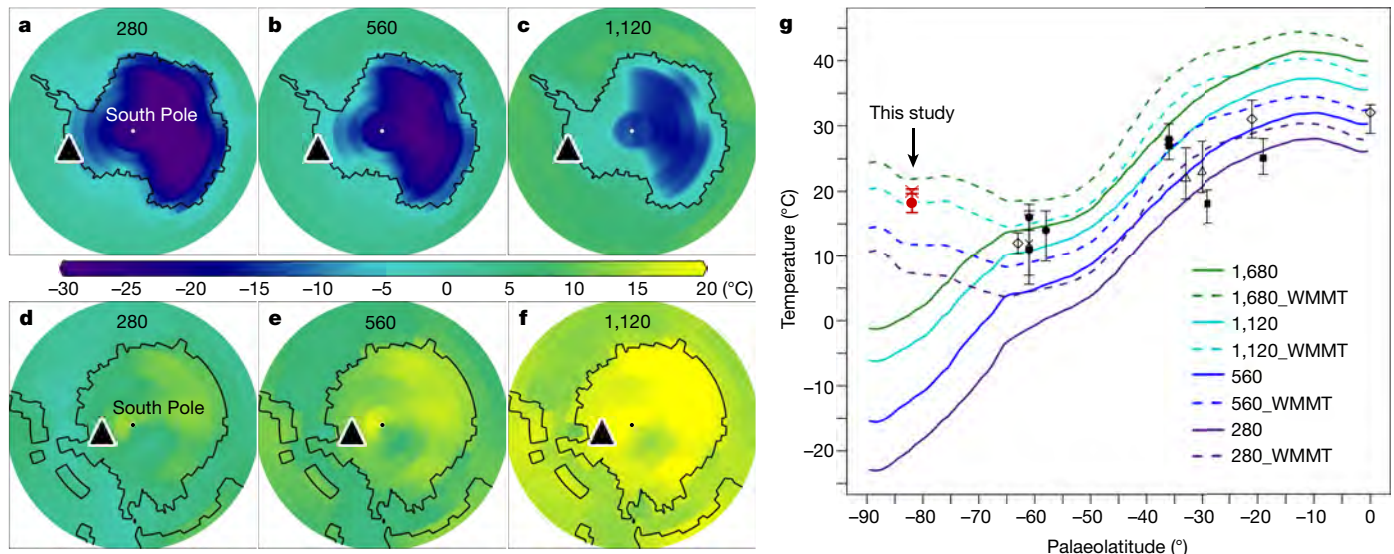


Fig. 4 | Modern and mid-Cretaceous CO₂ sensitivity runs. **a–f**, Distribution of warmest mean month temperatures (WMMT, colour scale) for present-day (**a–c**) and mid-Cretaceous at 90 Ma (**d–f**) configurations under atmospheric CO₂ levels of 280, 560 and 1,120 ppmv (representing 1×, 2× and 4× PI CO₂). The black triangle indicates the approximate position of site PS104_20-2. **g**, Modelled mid-Cretaceous WMMT (dashed lines) and zonal mean temperatures (solid lines) for different atmospheric CO₂ concentrations. The

temperature estimates (data points), including their respective calibration error (2σ), were derived from the following proxies referred to in ref. 5: terrestrial $\delta^{18}\text{O}$ of vertebrate tooth enamel and/or pedogenic carbonate (filled squares), palaeobotanical data (filled circles), fish enamel $\delta^{18}\text{O}$ (open triangles), marine calcareous fossil $\delta^{18}\text{O}$ (open diamonds) and biomarkers (cross). Temperature estimates from this study are indicated by a red filled circle (palaeobotany) and red cross (HG palaeothermometry).

around 1,120 mm yr⁻¹. The average temperature of the warmest summer month was 18.5 °C. Previous quantitative climate analyses from Antarctic records ~2,500 km further north resulted in Coniacian–Santonian (–89–84 Ma) mean annual air temperatures of 15–21 °C (refs. 47,48), suggesting a shallow temperature gradient towards our site. Estimates of the Late Cretaceous climate based on NLRs generally agree well with other temperature proxies⁴⁷. However, the approach assumes similarity of climate requirements for fossil taxa and their NLRs. With increasing age, the phylogenetic relationships of a fossil taxon become more disparate and the assumption thus becomes less robust. We therefore applied an independent geochemical palaeothermometer (HTI₃₀) based on the distribution of the heterocyst glycolipids (ref. 49), which corroborated our bioclimatic reconstructions by indicating austral summer lake or river-surface water temperatures of –20 °C for the swampy rainforest (Extended Data Fig. 4; see Methods). Our record contains, to our knowledge, the hitherto southernmost evidence of Cretaceous terrestrial environmental conditions and reveals a mid-Cretaceous ‘greenhouse climate’ that was capable of maintaining temperate conditions much farther south than previously documented¹⁴.

Palaeoclimate modelling

In light of extremely limited mid-Cretaceous CO₂ proxy data⁶ and widely scattered existing data estimates⁵, and to identify some of the pivotal driving mechanism of high-latitude mid-Cretaceous environmental conditions reconstructed for our new record, we ran the global climate model COSMOS⁵ in a coupled atmosphere–ocean configuration with fixed vegetation. We did so under present-day (Fig. 4a–c) and mid-Cretaceous configurations at 90 Ma (Fig. 4d–g) for 1×, 2×, 4× and 6× pre-industrial (PI) CO₂ levels of 280 ppmv (280, 560, 1,120 and 1,680 ppmv, respectively; see Methods). Although the model predicts a mid-Cretaceous climate in West Antarctica that is already warmer under PI CO₂ levels (Fig. 4d), summer surface air and water temperatures of –20 °C at –82° S can only be reproduced by forcing the climate with very high atmospheric CO₂ levels between 1,120 and 1,680 ppmv (Fig. 4f, g). Our reconstructed mean annual air temperature of 13 °C, however, still remains strongly underestimated by the model (Fig. 4g).

We conclude that a temperate climate at such a high latitude with more than four months of complete polar night darkness requires a combination of both strongly elevated atmospheric CO₂ concentrations and dense surface vegetation that generates a low planetary albedo with an associated high radiant energy absorption and pronounced seasonality. This largely precludes the existence¹⁰ of any substantial ice-sheet and sea-ice cover in and around Antarctica during the Turonian to Santonian stages of the Late Cretaceous epoch, an interpretation supported by palaeogeographic reconstructions of that period⁵⁰. Conversely, the present Antarctic Ice Sheet and its associated climate feedbacks, such as ice albedo, would provide a stabilizing cooling effect in a future high-CO₂ world (Fig. 4a–c).

To further elaborate on the importance of additional forcing mechanisms, to discover the interdependency of surface vegetation and temperature sensitivity in more detail and to explore the drivers of the paradox in the late Cretaceous latitudinal temperature gradient visible in Fig. 4, future work should aim to run the model with various types of vegetation cover coupled with other drivers such as palaeogeography⁵⁰ or changes in cloudiness⁵¹.

Our findings highlight the importance of including land–ice changes in long-term climate simulations to accurately estimate climate sensitivity on these extended timescales⁵². We provide key data for constraining the response of polar terrestrial ecosystems to very high atmospheric CO₂ concentrations and for assessing the impact of Antarctic ice sheet presence under high-CO₂ scenarios—both of which are essential for modelling past and future climate change⁵³.

Online content

Any methods, additional references, Nature Research reporting summaries, source data, extended data, supplementary information, acknowledgements, peer review information; details of author contributions and competing interests; and statements of data and code availability are available at <https://doi.org/10.1038/s41586-020-2148-5>.

1. Forster, A., Schouten, S., Baas, M. & Sinninghe Damsté, J. S. Mid-Cretaceous (Albian–Santonian) sea surface temperature record of the tropical Atlantic Ocean. *Geology* **35**, 919–922 (2007).
2. Forster, A. et al. Tropical warming and intermittent cooling during the Cenomanian/Turonian Oceanic Anoxic Event (OAE 2): sea surface temperature records from the equatorial Atlantic. *Paleoceanography* **22**, PA1219 (2007).
3. Tarduno, J. A. et al. Evidence for extreme climatic warmth from late Cretaceous Arctic vertebrates. *Science* **282**, 2241–2243 (1998).
4. O'Brien, C. L. et al. Cretaceous sea-surface temperature evolution: constraints from TEX₈₆ and planktonic foraminiferal oxygen isotopes. *Earth Sci. Rev.* **172**, 224–247 (2017).
5. Niezgodzki, I. et al. Late Cretaceous climate simulations with different CO₂ levels and subarctic gateway configurations: a model-data comparison. *Paleoceanography* **32**, 980–998 (2017).
6. Foster, G. L., Royer, D. L. & Lunt, D. J. Future climate forcing potentially without precedent in the last 420 million years. *Nat. Commun.* **8**, 14845 (2017).
7. O'Connor, L. K. et al. Late Cretaceous temperature evolution of the southern high latitudes: a TEX₈₆ perspective. *Paleoceanogr. Paleoclimatol.* **34**, 436–454 (2019).
8. Jenkyns, H. C., Forster, A., Schouten, S. & Sinninghe Damsté, S. High temperatures in the Late Cretaceous Arctic Ocean. *Nature* **432**, 888–892 (2004).
9. Ditchfield, P. W., Marshall, J. D. & Pirrie, D. High latitude palaeotemperature variation: new data from the Tithonian to Eocene of James Ross Island, Antarctica. *Palaeogeogr. Palaeoclimatol. Palaeoecol.* **107**, 79–101 (1994).
10. Bornemann, A. et al. Isotopic evidence for glaciation during the Cretaceous supergreenhouse. *Science* **319**, 189–192 (2008).
11. Müller, R. D. et al. Long-term sea-level fluctuations driven by ocean basin dynamics. *Science* **319**, 1357–1362 (2008).
12. Miller, K. G. et al. The Phanerozoic record of global sea-level change. *Science* **310**, 1293–1298 (2005).
13. McPhail, M. K. & Truswell, E. M. Palynology of Site 1166, Prydz Bay, East Antarctica. In *Proc. ODP Sci. Res. Vol. 188* (eds Cooper, A. K., O'Brien, P. E. & Richter, C.) 1–43 (Ocean Drilling Program, 2004).
14. Mays, C., Steinhilber, M. & Stilwell, J. D. Climatic implications of *Ginkgoites waarensis* Douglas emend. from the south polar Tupuangi flora, Late Cretaceous (Cenomanian), Chatham Islands. *Palaeogeogr. Palaeoclimatol. Palaeoecol.* **438**, 308–326 (2015).
15. Pujana, R. R., Raffi, M. E. & Olivero, E. B. Conifer fossil woods from the Santa Marta Formation (Upper Cretaceous), Brandy Bay, James Ross Island, Antarctica. *Cretac. Res.* **77**, 28–38 (2017).
16. Manfroi, J. et al. The first report of a Campanian palaeo-wildfire in the West Antarctic Peninsula. *Palaeogeogr. Palaeoclimatol. Palaeoecol.* **418**, 12–18 (2015).
17. Falcon-Lang, H. J., Cantrill, D. J. & Nichols, G. J. Biodiversity and terrestrial ecology of a mid-Cretaceous, high-latitude floodplain, Alexander Island, Antarctica. *J. Geol. Soc. Lond.* **158**, 709–724 (2001).
18. Wang, Y. et al. Paleo-CO₂ variation trends and the Cretaceous greenhouse climate. *Earth Sci. Rev.* **129**, 136–147 (2014).
19. Huber, B. T., MacLeod, K. G., Watkins, D. K. & Coffin, M. F. The rise and fall of the Cretaceous Hot Greenhouse climate. *Glob. Planet. Change* **167**, 1–23 (2018).
20. Gohl, K. et al. MeBo70 seabed drilling on a polar continental shelf: operational report and lessons from drilling in the Amundsen Sea Embayment of West Antarctica. *Geochem. Geophys. Geosyst.* **18**, 4235–4250 (2017).
21. Lowe, A. L. & Anderson, J. B. Reconstruction of the West Antarctic ice sheet in Pine Island Bay during the Last Glacial Maximum and its subsequent retreat history. *Quat. Sci. Rev.* **21**, 1879–1897 (2002).
22. Spiegel, C. et al. Tectonomorphic evolution of Marie Byrd Land—implications for Cenozoic rifting activity and onset of West Antarctic glaciation. *Glob. Planet. Change* **145**, 98–115 (2016).
23. Larter, R. D. et al. Reconstruction of changes in the Amundsen Sea and Bellingshausen Sea sector of the West Antarctic Ice Sheet since the Last Glacial Maximum. *Quat. Sci. Rev.* **100**, 55–86 (2014).
24. Gohl, K. et al. Seismic stratigraphic record of the Amundsen Sea Embayment shelf from pre-glacial to recent times: Evidence for a dynamic West Antarctic ice sheet. *Mar. Geol.* **344**, 115–131 (2013).
25. Freudenthal, T. & Wefer, G. Drilling cores on the sea floor with the remote-controlled sea floor drilling rig MeBo. *Geosci. Instrum. Methods Data Syst.* **2**, 329–337 (2013).
26. Crompton, J. S. et al. In *The New Zealand Geological Timescale Monograph 22* (ed. Cooper, R. A.) 103–122 (Institute of Geological and Nuclear Sciences, 2004).
27. Mays, C. & Stilwell, J. D. Pollen and spore biostratigraphy of the mid-Cretaceous Tupuangi Formation, Chatham Islands, New Zealand. *Rev. Palaeobot. Palynol.* **192**, 79–102 (2013).
28. Mildenhall, D. C. *Palynological Reconnaissance of Early Cretaceous to Holocene Sediments, Chatham Islands, New Zealand Monograph 7* (Institute of Geological & Nuclear Sciences, 1994).
29. He, T., Lamont, B. B. & Fogliani, B. Pre-Gondwanan-breakup origin of *Beauprea* (Proteaceae) explains its historical presence in New Caledonia and New Zealand. *Sci. Adv.* **2**, e1501648 (2016).
30. Gee, J. & Kent, D. in *Treatise on Geophysics* Vol. 5 (ed. Kono, M.) Ch. 5.12 (Elsevier, 2007).
31. Wobbe, F., Gohl, K., Chambord, A. & Sutherland, R. Structure and breakup history of the rifted margin of West Antarctica in relation to Cretaceous separation from Zealandia and Bellingshausen plate motion. *Geochem. Geophys. Geosyst.* **13**, Q04W12 (2012).
32. Jordan, T. A., Riley, T. R. & Siddoway, C. S. The geological history and evolution of West Antarctica. *Nat. Rev. Earth Environ.* **1**, 117–133 (2020).
33. Müller, R. D. et al. GPlates: building a virtual Earth through deep time. *Geochem. Geophys. Geosyst.* **19**, 2243–2261 (2018).
34. DiVenere, V. J., Kent, D. V. & Dalziel, I. W. D. Mid-Cretaceous paleomagnetic results from Marie Byrd Land, West Antarctica: a test of post-100 Ma relative motion between East and West Antarctica. *J. Geophys. Res.* **99** (B8), 15115–15139 (1994).
35. Pocknall, D. T. & Crosbie, Y. M. Pollen morphology of *Beauprea* (Proteaceae): modern and fossil. *Rev. Palaeobot. Palynol.* **53**, 305–327 (1988).
36. Jackson, M. B. & Armstrong, W. Formation of aerenchyma and the processes of plant ventilation in relation to soil flooding and submergence. *Plant Biol.* **1**, 274–287 (1999).
37. Lijmbach, G. W. M. On the origin of petroleum. In *Proc. 9th World Petroleum Congress Vol. 2*, 357–369 (World Petroleum Congress, 1975).
38. Peters, K. E., Walters, C. C. & Moldovan, J. M. *The Biomarker Guide* (Cambridge Univ. Press, 2004).
39. Meyers, P. A. Applications of organic geochemistry to paleolimnological reconstructions: a summary of examples from the Laurentian Great Lakes. *Org. Geochem.* **34**, 261–289 (2003).
40. Robert, C. & Kennett, J. P. Antarctic subtropical humid episode at the Paleocene–Eocene boundary: clay-mineral evidence. *Geology* **22**, 211–214 (1994).
41. Huang, W. H. & Keller, W. D. Dissolution of rock-forming silicate minerals in organic acids: simulated first-stage weathering of fresh mineral surfaces. *Am. Mineral.* **55**, 2076–2094 (1970).
42. Sugden, D. E. & Jamieson, S. S. R. The pre-glacial landscape of Antarctica. *Scott. Geogr. J.* **134**, 203–223 (2018).
43. Uenzelmann-Neben, G. & Gohl, K. Early glaciation already during the Early Miocene in the Amundsen Sea, Southern Pacific: indications from the distribution of sedimentary sequences. *Glob. Planet. Change* **120**, 92–104 (2014).
44. Zundel, M. et al. Thurston Island (West Antarctica) between Gondwana subduction and continental separation: A multistage evolution revealed by apatite thermochronology. *Tectonics* **38**, 878–897 (2019).
45. Müller, R. D., Gohl, K., Cande, S. C., Goncharov, A. & Golynsky, A. V. Eocene to Miocene geometry of the West Antarctic rift system. *Aust. J. Earth Sci.* **54**, 1033–1045 (2007).
46. Harbert, R. S. & Nixon, K. C. Climate reconstruction analysis using coexistence likelihood estimation (CRACLE): a method for the estimation of climate using vegetation. *Am. J. Bot.* **102**, 1277–1289 (2015).
47. Poole, I., Cantrill, D. J. & Utescher, T. Reconstructing Antarctic palaeoclimate from wood floras: a comparison using multivariate anatomical analysis and the coexistence approach. *Palaeogeogr. Palaeoclimatol. Palaeoecol.* **222**, 95–121 (2005).
48. Francis, J. E. et al. 100 million years of Antarctic climate evolution: evidence from fossil plants. In *Proc. 10th Int. Symp. on Antarctic Earth Sciences* (eds Cooper, A. K. et al.) 19–27 (National Academies, 2007).
49. Bauersachs, T., Rochelmeier, J. & Schwark, L. Seasonal lake surface water temperature trends reflected by heterocyst glycolipid-based molecular thermometers. *Biogeosciences* **12**, 3741–3751 (2015).
50. Ladant, J. L. & Donnadieu, Y. Paleogeographic regulation of glacial events during the Cretaceous supergreenhouse. *Nat. Commun.* **7**, 12771 (2016).
51. Upchurch, G. R., Jr, Kiehl, J., Shields, C., Scherer, J. & Scotese, C. Latitudinal temperature gradients and high-latitude temperatures during the latest Cretaceous: congruence of geologic data and climate models. *Geology* **43**, 683–686 (2015).
52. Farnsworth, A. et al. Climate sensitivity on geological timescales controlled by non-linear feedbacks and ocean circulation. *Geophys. Res. Lett.* **46**, 9880–9889 (2019).
53. *IPCC Special Report on the Ocean and Cryosphere in a Changing Climate* (eds Pörtner, H. O. et al.) (IPCC, 2019); https://www.ipcc.ch/site/assets/uploads/sites/3/2019/12/SROCC_FullReport_FINAL.pdf
54. Arndt, J. E. et al. A new bathymetric compilation covering circum-Antarctic waters. *Geophys. Res. Lett.* **40**, 3111–3117 (2013).
55. Fretwell, P. et al. Bedmap2: improved ice bed, surface and thickness datasets for Antarctica. *Cryosphere* **7**, 375–393 (2013).

Publisher's note Springer Nature remains neutral with regard to jurisdictional claims in published maps and institutional affiliations.

© The Author(s), under exclusive licence to Springer Nature Limited 2020

Science Team of Expedition PS104

V. Afanasyeva¹⁶, J. E. Arndt¹, B. Ebermann¹⁷, C. Gebhardt¹, K. Hochmuth¹⁸, K. Küssner¹, Y. Najman¹⁸, F. Riefstahl¹ & M. Scheinert¹⁷

¹⁶VNIOkeangeologie, St Petersburg, Russia. ¹⁷Technische Universität Dresden, Dresden, Germany. ¹⁸Lancaster Environment Centre, Lancaster University, Lancaster, UK. ¹⁹Present address: School of Geology, Geography & the Environment, University of Leicester, Leicester, UK.

Methods

Seafloor drill rig MARUM-MeBo70

MARUM-MeBo70 is a robotic drill rig that was deployed on the seabed and remotely controlled from RV *Polarstern* during expedition PS104²⁰. Detailed information about the drill rig and its operation is published in ref.²⁵.

X-ray CT

Whole rounds of MeBo core PS104_20-2 were scanned by a Toshiba Aquilion 64 computer tomograph at the hospital Klinikum Bremen-Mitte, with an X-ray source voltage of 120 kV and a current of 600 mA. The CT scans have a resolution of 0.351 mm in x and y directions and 0.5 mm resolution in the z direction (resolution of scaled reconstruction: 0.195 × 0.195 × 0.3 mm³). Images were reconstructed using Toshiba's patented helical cone beam reconstruction technique. The obtained CT data were processed using the ZIB edition of the Amira software (version 2017.39)⁵⁶. Within Amira, the CT scans of the core sections were merged when necessary and core liners, including about 2 mm of the core rims, were removed from the dataset until all marginal artefacts from the coring process were removed. Subsequently, all clasts larger than -1 mm, root-traces (where present) and matrix sediment were segmented with the (marker-based) watershed tool of the Segmentation Editor. Markers were predominantly set with the threshold tool. For only rarely occurring clasts with an X-ray attenuation close to the matrix sediment, the magix wand tool was used to manually set additional markers. Holes within clasts after the watershed segmentation were added to the clasts with the selection fill tool.

Palynology

Between 2 and 6 g of dry-weight sediment per sample were processed at Northumbria University following standard palynological techniques, including sieving (10 µm) and acid treatment with 10% HCl (hydrochloric acid) and cold 38% HF (hydrofluoric acid). The processed residue was transferred to microscope slides using glycerine jelly as a mounting medium, and 2–3 slides were analysed per sample at 400× magnification. Of the 17 samples analysed for pollen and spores, 7 were productive, and total counts range from 340 to 360 pollen grains and spores per sample (Extended Data Figs. 2, 3; Extended Data Table 1). Pollen concentrations increase from an average of ~6,500 grains per gram of sediment in the lower three samples to 61,000–121,500 g⁻¹ at the top. We could not identify any reworking of palynomorphs. Percentages were calculated on the basis of the sum total of pollen and spores; 65 pollen and spore taxa were identified from the literature^{57–59} (Extended Data Table 3). All samples contained a high morphological diversity of *Podocarpus* pollen, which we classified as *Podocarpidites* undiff. as many of these grains were either folded or damaged and were therefore unidentifiable beyond family level. Marine dinoflagellate cysts were absent in all samples.

Palynomorph-based climate reconstructions (bioclimatic analysis)

We reconstructed terrestrial mean annual temperature (MAT), precipitation (MAP) and WMMT using the NLR approach. The NLR approach uses the climatic requirements of the NLR of fossil taxa to reconstruct the past climatic range and assumes that the climatic requirements of the fossil taxa are similar to those of their NLR (Extended Data Table 2). NLR approaches use the presence or absence of individual taxa in a fossil assemblage rather than relative abundance, which reduces the likelihood of taphonomic biases. This facilitates, to some extent, the reconstruction of past, non-modern analogue climates and environments⁶⁰. NLR-based temperature estimates are generally in good agreement with estimates from geochemical and other palaeobotanical methods, including the Climate Leaf Analysis Multivariate

Program (CLAMP) and leaf margin analysis^{61–67}, providing confidence in the utility of the method for the reconstruction of pre-Quaternary climates.

However, quantitative climate estimates from the fossil plant record of deep-time geological intervals are always accompanied by large uncertainties. Incorrect use of outliers and fossil taxa with ambiguous affinity can result in erroneous climate estimates⁶⁸. One of the greatest weaknesses that affects all NLR approaches is the assumption of uniformitarianism—namely, that the climate tolerances of modern species can be extended into the past. This assumption inevitably introduces uncertainty that increases with the age of the geological formation⁶⁹. To statistically constrain the most likely climatic co-occurrence envelope, we combined the NLR approach with the probability density function (PDF) method^{46,70,71}. In contrast to other NLR methods, such as the coexistence approach, the PDF method has the advantage that it statistically constrains the most likely climatic co-occurrence envelope, thereby offering a solution that mathematically reduces the potential impact of wrongly defined climate tolerance on upper and lower limits of palaeoclimatic estimates. To further reduce uncertainties caused by potentially wrong identification of NLR, we removed fossil taxa with potentially ambiguous affinity or very rare occurrence in the fossil record (Extended Data Table 2). This includes *Microcachrydites antarcticus*, a taxon abundant and widespread in the Antarctic fossil record, with the NLR *Microcachrys tetragona* (the sole species of the genus *Microcachrys* that is now endemic to Tasmania). Another example is *Peninsulapollis gillii* with close links to the modern genus *Beauprea*, and endemic to New Caledonia. In both cases we used the family, Podocarpaceae and Proteaceae, respectively, rather than the genus or species as the NLR.

To generate the paleoclimate estimate, we followed the procedure described in refs.^{59,63}. We first identified the bioclimatic envelope for each NLR by cross-plotting their modern distribution from the Global Biodiversity Information Facility (GBIF)⁷² with the gridded WorldCLIM climate surface⁷³ using the dismo package⁷⁴ in R. We then filtered the dataset and removed redundant data, 'exotic' occurrences (such as garden plants) as well as multiple entries per climate grid cell to avoid the climatic probability function becoming highly slanted towards that location⁷⁵. Before establishing the PDFs, bootstrapping was applied to test the robustness of the dataset, which is of particular interest for taxa with only few modern occurrences. Following the bootstrapping, we calculated the likelihood (f) of a taxon (t) occurring at value (x) for a certain climatic variable by using the mean (μ) and standard deviation (σ) of the modern distribution range of each taxa^{65,70}.

$$f(x)_t = \frac{1}{\sqrt{2\pi\sigma_x^2}} e^{-\frac{(x-\mu_x)^2}{2\sigma_x^2}}$$

Because the separate reconstruction of climate ranges for each variable can lead to bioclimatic envelopes that include intervals, where no modern-day occurrence of t is observed⁶⁵, we calculated joint likelihood PDFs for each combination of the climate variables MAT, MAP and WMMT using the correlation coefficient $p(x, y)$:

$$f(x, y)_t = \frac{1}{2\pi\sigma_x\sigma_y\sqrt{1-p^2}} e^{-\frac{1}{2(1-p^2)}\left(\frac{(x-\mu_x)^2}{2\sigma_x^2} + \frac{(y-\mu_y)^2}{2\sigma_y^2} - 2p\frac{(x-\mu_x)(y-\mu_y)}{\sigma_x\sigma_y}\right)}$$

After assessing whether all bioclimatic envelopes share a coexistence interval, the climate estimates of the NLR assemblage were reconstructed by multiplying the individual joint likelihoods of taxa $f(x, y)_{t1} \dots f(x, y)_{tn}$ with each other:

$$f(x, y)_{\text{Combined}} = f(x, y)_{t1} \times f(x, y)_{t2} \times \dots \times f(x, y)_{tn}$$

To constrain the core distribution of a group, we determined the range of one ($f(x, y)_{\text{relative}} = 0.157$) and two standard deviations ($f(x, y)_{\text{relative}} = 0.023$) from the occurrence within a group with $f(x, y)_{\text{max}}$ representing the most likely climate conditions⁷⁵.

$$f(x, y)_{\text{relative}} = \frac{f(x, y)}{f(x, y)_{\text{max}}}$$

For our bioclimatic analysis, we used all pollen and spore taxa that could be related to an NLR (following ref.⁵⁹, Extended Data Table 2). Climatic ranges are indicated with their $\pm 2\sigma$ range. We calculated an MAT of 12.8 ± 2.2 °C, WMMT of 18.4 ± 1.9 °C and MAP of $1,120 \pm 330$ mm yr⁻¹. It should be noted that the ranges of these values show the mathematical error and not the real range, which might result from the uncertainties in using an NLR approach. To avoid misunderstandings, we therefore indicated in the main text the pollen-based climate estimates without 2σ ranges.

Organic geochemistry

Freeze-dried and homogenized sediment samples were extracted by means of ultrasonication using a dichloromethane:methanol mixture (2:1, v-v). After centrifugation, the total lipid extract was dried by rotary evaporation. The extraction was repeated twice. The combined total lipid extract was fractionated using silica open-column chromatography and hexane as eluent to obtain apolar lipids. Hydrocarbons were analysed using an HP gas chromatograph 6890 (30 m DB-5MS column, 0.25 mm diameter, 0.25 µm film thickness). The identification of *n*-alkanes, pristane and phytane was based on comparison of their retention times with those of reference compounds that were run on the same instrument. The TAR⁷⁶ was calculated using peak areas of long-chain (*n*-C₂₇, *n*-C₂₉, *n*-C₃₁) against short-chain (*n*-C₁₅, *n*-C₁₇, *n*-C₁₉) alkanes. The carbon preference index (CPI) was calculated as follows³⁸:

$$\text{CPI} = \frac{2 \times (n\text{-C}_{23} + n\text{-C}_{25} + n\text{-C}_{27} + n\text{-C}_{29})}{n\text{-C}_{22} + 2 \times (n\text{-C}_{24} + n\text{-C}_{26} + n\text{-C}_{28}) + n\text{-C}_{30}} \quad (1)$$

Heterocyst glycolipid palaeothermometry

Sediment samples from the coastal sandstone (9R, 50–52 cm; 26.76 mbsf) and the carbonaceous mudstone (9R, 76.5–78 cm; 27.02 mbsf; 10R, 60–62 cm; 29.21 mbsf) were lyophilized and ground to a fine sediment powder using a solvent-cleaned agate pestle and mortar. Between 20.1 and 29.7 g of sediment were extracted using a modified Bligh and Dyer procedure⁷⁷. Briefly, sediment samples were extracted ultrasonically (for 10 min.) three times in a solvent mixture of MeOH, DCM and phosphate buffer (2:1:0.8; v-v:v). After each sonication step, the solvent mixture was centrifuged at 1,500g for 3 min and the supernatant transferred to a centrifuge tube. The combined supernatants were phase separated by adding DCM and phosphate buffer to a final solvent ratio of 1:1:0.9 (v:v:v). The organic bottom layer was collected in a round bottom flask and reduced under vacuum using a rotary evaporator. Each Bligh and Dyer extract (BDE) was transferred to a preweighed vial using DCM:MeOH (1:1, v-v) and dried under a gentle stream of N₂. Before analysis, all BDEs were redissolved in a solvent mixture of *n*-hexane:2-propanol:H₂O (72:27:1; v-v:v) to a concentration of 8 mg ml⁻¹. A procedural blank was added to the sample batch and treated as a regular sample to test for possible cross-contamination during sample preparation.

High-performance liquid chromatograph coupled to electrospray ionisation tandem mass spectrometry (HPLC/ESI-MS²) was performed on the BDEs following the analytical procedure given by ref.⁷⁸ to establish heterocyst glycolipid (HG) distribution patterns and determine relative abundances. Separation of HGs was achieved using a Waters Alliance 2690 HPLC system fitted with a Phenomenex Luna NH₂ column (150 × 2 mm²; 3 µm particle size) and a guard column of the same

material. Both were maintained at a constant temperature of 30 °C. The applied gradient profile was as follows: 95% A:5% B to 85% A:15% B in 10 min. (isocratic for 7 min) at 0.5 ml min⁻¹, followed by back flushing with 30% A:70% B at 0.2 ml min⁻¹ for 25 min and re-equilibrating the column with 95% A:5% B for 15 min. Solvent A was *n*-hexane:2-propanol:HCO₂H:14.8 MNH₃ aq. (79:20:0.12:0.04; v-v:v:v) and Solvent B was 2-propanol:water:HCO₂H:14.8 MNH₃ aq. (88:10:0.12:0.04; v-v:v:v).

HGs were detected using a Micromass Quattro LC triple quadrupole mass spectrometer equipped with an electrospray ionization interface and operated in positive ion mode. Source conditions were as given in ref.⁷⁹. All BDEs were analysed in multiple reaction monitoring mode to achieve maximum specificity. HGs were identified on the basis of a comparison of retention times with those of HGs in cultured cyanobacteria, as well as published mass spectra^{80–84}. HGs were monitored using the following transitions: *m/z* 547 → 415 (pentose HG₂₆ diol), *m/z* 603 → 471 (pentose HG₃₀ diol), *m/z* 619 → 487 (pentose HG₃₀ triol), *m/z* 647 → 515 (pentose HG₃₂ triol), *m/z* 561 → 415 (deoxyhexose HG₂₆ diol), *m/z* 575 → 413 (HG₂₆ keto-ol), *m/z* 577 → 415 (HG₂₆ diol), *m/z* 603 → 441 (HG₂₈ keto-ol), *m/z* 605 → 443 (HG₂₈ diol), *m/z* 619 → 457 (HG₂₈ keto-diol), *m/z* 621 → 459 (HG₂₈ triol), *m/z* 635 → 459 (methylated hexose HG₂₈ triol), *m/z* 647 → 485 (HG₃₀ keto-diol), *m/z* 649 → 487 (HG₃₀ triol), *m/z* 675 → 513 (HG₃₂ keto-diol), *m/z* 677 → 515 (HG₃₂ triol) and quantified by integrating peak areas using the QuanLynx application software (version 4.1 SCN856).

Surface water temperatures (SWTs) during the deposition of the coastal Eocene sandstone were reconstructed using the HDI₂₆ (heterocyst diol index of 26 carbon atoms) and HDI₂₈ (HDI of 28 carbon atoms) lipid palaeothermometers as described in ref.⁴⁹. As the HG content of the swampy palaeoenvironment exclusively consisted of HG₃₀ triols and HG₃₀ keto-diol (Extended Data Fig. 4), which are specific to cyanobacteria that form benthic microbial mats⁸², we here applied the HTI₃₀ (heterocyst triol index of 30 carbon atoms) to the mudstone sequence. This index is defined as follows:

$$\text{HTI}_{30} = \text{HG}_{30} \text{ triol} / (\text{HG}_{30} \text{ triol} + \text{HG}_{30} \text{ keto-diol})$$

The HTI₃₀ was transferred to absolute temperatures using a surface sediment calibration obtained from a large set of East African lakes (*n* = 47) located on an altitudinal transect from 615 to 4,504 m above sea level with SWTs ranging from 5.7 to 27.9 °C. In this setting, the HTI₃₀ showed a strong linear correlation with SWT, which is expressed in the equation below (T.B., unpublished data):

$$\text{SWT} = (\text{HTI}_{30} / 0.0249) - (0.2609 / 0.0249)$$

Independent confirmation for the robustness of the HG-based temperature reconstruction is obtained by comparing HG distribution patterns and HTI₃₀ values in the mudstone sequence with those reported for an axenic culture of the heterocystous cyanobacterium *Scytonema* sp. PCC (Pasteur Culture collection of Cyanobacteria) 10023 (ref.⁸⁴). This cyanobacterium exclusively contains HG₃₀ triols and HG₃₀ keto-diols. The above transfer function yields an HTI₃₀ value of -0.88 for the culture grown at an ambient temperature of 25 °C. This value is identical to the HTI₃₀ (0.88) calculated using the relative abundances of the major HG₃₀ triol and HG₃₀ keto-diol isomers reported in ref.⁸⁴.

Grain-size analyses

A set of discrete samples was wet sieved at 2 mm and 63 µm to separate the gravel, sand and mud grain-size classes. The <63 µm (mud) suspension was separated into silt (2–63 µm) and clay (<2 µm) using settling velocity (Stokes' Law) in Atterberg tubes.

Clay mineral analyses

An aliquot of the clay fraction was used to determine the relative contents of the clay minerals smectite, illite, chlorite and kaolinite using an automated powder diffractometer system Rigaku MiniFlex with Co

K α radiation (30 kV, 15 mA) at the Institute for Geophysics and Geology (University of Leipzig). The clay mineral identification and quantification followed standard X-ray diffraction methods⁸⁵.

Bulk sediment composition

Total carbon (TC) and total nitrogen (TN) contents were analysed with an Elementar Vario EL III. The TOC contents were determined after removal of the total inorganic carbon (carbonates) with HCl using an ELTRA CS-2000. Carbonate content was calculated by subtracting the TOC from the TC and multiplying the difference (total inorganic carbon) by 8.33; that is, the ratio between the molecular weights of CaCO₃ and C. The TOC:TN (C:N) ratio was calculated on a molar basis.

The mineralogical composition of the milled bulk sediment was analysed semiquantitatively with X-ray diffraction using peak intensities and area ratios analysed with the MacDiff program (version 4.2.6).⁸⁶ For the Fe(Ca) carbonates the peak intensities for ankerite (at 2.906 Å) and siderite (at 2.795 Å) were used and summed up as percentages for Fe(Ca) carbonates (ankerite and siderite) in relation to the absolute percentage of other carbonates (calcite, Mg calcite and dolomite).

Thin sections

After drying the untreated soft sediment in the fridge for 2–3 days, the sediment was dried at room temperature (20–22 °C) for another 2–3 days. During that time the sediment was checked daily for crack formation. Under low pressure, the sediment was impregnated stepwise in a vacuum exicator with epoxy araldite 2020 resin until full coverage of the sample was achieved. After complete hardening, the bottom of the sample was ground by a Tegrapol with silicon carbide (SiC) paper sizes from 80 to 800—depending on sediment characteristics—and a maximum of 150 rotations per minute until the sediment surface was reached. The glass slides for the thin sections, which were 3 mm thick and 35 × 120 mm in area, were ground with a 9- μ m-fraction SiC paper to achieve both grip and an even surface (alternative machine system: Logitech LP50 auto). Then the sample was attached to the slide with the same resin used for impregnation by a pressure block. Afterwards, the surface of the glass was cleaned and labelled with a diamond pen. Most samples were then cut by a WOCO 50 diamond saw to achieve 250- μ m-thick sediment strips on the glass, before grinding with SiC paper or the Logitech LP50 to reach a thickness of 30 μ m. Only some sections were covered with 150- μ m-thick glasses, for which an ultraviolet resin (cyanacrylate) was used. Most sections remained uncovered for Raman and SEM-EDX spectroscopy. Finally, all thin sections were cleaned with ethanol. The set of thin sections was prepared by MKfactory.

Palaeomagnetic measurements

Five discrete samples were taken at variable spacings from cores 9R and 10R of core PS104_20-2 for palaeomagnetic investigations using plastic boxes with inner dimensions of 2 × 2 × 2 cm³. The directions and intensities of natural remanent magnetization were measured on a cryogenic magnetometer (model 2G Enterprises 755 HR). Subsequent alternating field (AF) demagnetization of natural remanent magnetization involved 15 steps to a maximum AF intensity of 100 mT. A detailed vector analysis⁸⁷ was applied to the results to determine the characteristic remanent magnetization of each sample and to unravel its magnetic polarity. Samples showing no systematic demagnetization pattern were excluded from further interpretation.

Palaeoclimate modelling

We use the COSMOS model (see Code availability) in a coupled atmosphere–ocean configuration with fixed vegetation. The atmosphere component ECHAM5 is run in a T31/L19 resolution⁸⁸. It consists of 19 vertical layers and has a horizontal resolution of ~3.75°. The ocean component MPI-OM runs in a GR30/L40 configuration⁸⁹. It has a formal horizontal resolution of 3.0° × 1.8° and consists of 40 unequal vertical

layers. The high-resolution hydrological discharge model is a part of ECHAM5⁹⁰, while MPI-OM includes a dynamic–thermodynamic sea-ice model using a viscous–plastic rheology⁹¹. Climate simulations were run for present-day and mid-Cretaceous configurations under different CO₂ levels in the atmosphere. Other greenhouse gases (such as CH₄ and N₂O) were set to PI levels. In the mid-Cretaceous simulations, we employed published paleogeography⁹² and vegetation⁹³ as well as no ice sheets in both hemispheres. The orbital configurations in all Cretaceous experiments were fixed at 800 common era (CE) and hence represent values from the beginning of externally forced simulation from 800 to 1800 CE (a so-called millennial run). The solar constant was reduced by 1% for the mid-Cretaceous experiments relative to the present-day value. The simulations with 1× and 2× PI CO₂ levels were run for 9,200 and 9,000 years, respectively, and 10,600 years for 4× PI CO₂ (ref. ⁹⁴). All simulations reached equilibrium at the surface. The experiment with a 6× PI CO₂ level had a slightly different atmospheric land–sea mask than the other three simulations. It was run for ~500 years and was not in a full equilibrium at the surface⁵. The PI control simulation was run for ~7,500 years. The simulations with 2× and 4× PI CO₂ levels were branched off from the 1× PI simulation from model year 6,800 and were further run for 700 years. The simulations reach either full or quasi-equilibrium at the surface. For the analyses the mean was taken over the last 100 years of each simulation. The model has been successfully applied previously for scientific questions focusing on the Quaternary^{95,96}, Neogene^{97–99}, Palaeogene^{100,101} and Late Cretaceous⁵, as well as estimates of future climate^{99,102}.

Sr and Nd isotopic measurements

A total of seven samples were selected for processing from cores 9R and 10R at site PS104_20-2. A detailed method description that was applied for determining their Sr and Nd isotopic compositions is given in ref. ¹⁰³.

Zircon and apatite U–Pb geochronology

The youngest detrital zircon and apatite U–Pb ages obtained from the cores 2R (sample AWI-35 at 9.9 mbsf) and 9R (sample AWI-25 at 26.7 mbsf) were used for constraining maximum deposition ages of the sandstone. The samples yielded Eocene apatite ($n = 2$) and zircon ($n = 1$) ages. The single Eocene zircon grain yields a Concordia age of 45.5 ± 2.0 Myr (Extended Data Fig. 1a). The apatite grains all yield analyses discordant in U–Pb isotopic space due to the presence of common Pb (Pb_c; that is, Pb incorporated during crystallization as opposed to radiogenic Pb* generated in situ by radionuclide decay). For single-grain ages, a terrestrial Pb isotope evolution model¹⁰⁴ was used for an initial estimate of ²⁰⁷Pb/²⁰⁶Pb_c, followed by an iterative approach to the ²⁰⁷Pb-based corrected age calculation¹⁰⁵.

As only two Eocene single-grain apatite ages are reported, the calculation of an array age would not normally be appropriate. However, comparison of the trace element chemistry (REE–Sr–Y) to an apatite compositional reference library¹⁰⁶ indicates that both Eocene grains are chemically, as well as chronologically, indistinguishable (Extended Data Fig. 1b), increasing the likelihood of a common source. Therefore, the two youngest apatite grains from AWI-35 were jointly regressed with the range of ²⁰⁷Pb/²⁰⁶Pb_c values (0.834 ± 0.018) for West Antarctic crystalline basement¹⁰⁷ (Extended Data Fig. 1a) to obtain a lower-intercept age of 39.3 ± 3.8 Myr (mean standard weighted deviation, MSWD = 0.99), similar to the independently obtained single-grain Concordia age of 45.5 ± 2.0 Myr determined from the youngest zircon from AWI-25. A Lutetian maximum deposition age (approximately 43 Myr) for AWI-35 and AWI-25 is therefore indicated.

Pure apatite and zircon separates were hand-picked from the non-magnetic heavy mineral 63–315 μ m size fraction, mounted in epoxy resin, ground to reveal internal surfaces and polished. Almost no sample bias was introduced by grain selection because in most cases all of the observed mineral grains were picked as the amount of sample material was very small. All U–Pb analyses were carried out using a Photon

Article

Machines Analyte Excite 193 nm ArF excimer laser-ablation system with a HelEx 2-volume ablation cell coupled to an Agilent 7900 ICPMS at the Department of Geology, Trinity College Dublin. Laser fluence was 2.5 J cm^{-2} with a repetition rate of 15 Hz and an analysis time of 20 s, followed by an 8 s pause to allow for signal wash-out and a subsequent baseline measurement. Spot sizes of $47 \mu\text{m}$ and $24 \mu\text{m}$ were employed for apatite and zircon respectively, in separate analytical sessions.

Data reduction employed the VizualAge and VizualAge_UComPbine data reduction schemes (DRS) for Lolite for zircon and apatite, respectively^{108–110}. Each DRS corrects for intrasession analytical drift, mass bias and downhole fractionation using a user-specified fractionation model based on measurements of the primary standard; VizualAge_UComPbine also permits the presence of a variable Pb_c content in a primary age standard that must be corrected using a known initial $^{207}\text{Pb}/^{206}\text{Pb}_c$ value. Final U–Pb age calculations were made using the Isoplot add-in for Excel¹¹¹.

Single-grain zircon U–Pb Concordia ages were calculated, and analyses with a probability of concordance <0.001 were rejected¹¹¹. The primary standard was Plešovice zircon; the GZ7 and 91,500 zircons were used as secondary standards and treated as unknowns during data reduction and age calculation¹¹², yielding Concordia ages of $530.1 \pm 3.7 \text{ Myr}$ and $1,060.4 \pm 6.8 \text{ Myr}$, respectively.

For apatite analyses, Madagascar apatite was employed as the primary standard and McClure Mountain and Durango apatites were employed as secondary standards^{113,114}. The Pb_c value in the secondary standards was corrected using fixed initial ratios, yielding weighted mean ages of $532.2 \pm 6.0 \text{ Myr}$ and $32.3 \pm 0.7 \text{ Myr}$, respectively. Variable Pb_c contents in the detrital apatite unknowns were corrected by using a terrestrial Pb evolution model¹⁰³ for the calculation of single-grain ages followed by an iterative calculation to obtain single-analysis ^{207}Pb -corrected ages¹⁰⁴. Alternatively, the range of the $^{207}\text{Pb}/^{206}\text{Pb}_c$ values for West Antarctic basement¹⁰⁵ can be used for the single-grain age calculation: the resulting single-grain ages are within 1 Myr of the single-grain ages obtained using the iterative calculation. Apatite U–Pb age filtering¹¹⁵ results in 2σ errors of $\leq 50\%$ for grains with ages of 10–100 Myr and 2σ errors of $\leq 25\%$ for grains with ages $>100 \text{ Myr}$. For apatite trace-element analysis, the lolite Trace Elements DRS was used. NIST612 glass and Madagascar apatite¹¹⁶ were employed as the primary and secondary reference materials respectively, with ^{43}Ca as an internal elemental standard¹¹⁷.

Data availability

All data are available online via PANGAEA at <https://doi.org/10.1594/PANGAEA.906092>.

Code availability

The standard model code of the ‘Community Earth System Models’ (COSMOS) version COSMOS-landveg r2413 (2009) is available upon request from the Max Planck Institute for Meteorology (Reinhard. Budich@mpimet.mpg.de). Analytical scripts are available via PANGAEA at <https://doi.org/10.1594/PANGAEA.910179>.

56. Stalling, D., Westerhoff, M. & Hege, H.-C. in *The Visualization Handbook* (eds Hansen, C. D. & Johnson, C. R.) 749–767 (Elsevier, 2005).
57. Raine, J. I., Mildenhall, D. C. & Kennedy, E. M. *New Zealand Fossil Spores and Pollen: An Illustrated Catalogue* 4th edn Science Miscellaneous Series Vol. 4 (GNS, 2011); <http://data.gns.cri.nz/sporepollen/index.htm>
58. Mays, C. A late Cretaceous (Cenomanian-Turonian) south polar palynoflora from the Chatham Islands, New Zealand. *Mem. Assoc. Aust. Palaeontol.* **47**, 92 (2015).
59. Bowman, V. C., Francis, J. E., Askin, R. A., Riding, J. B. & Swindles, G. T. Latest Cretaceous-earliest Paleogene vegetation and climate change at the high southern latitudes: palynological evidence from Seymour Island, Antarctic Peninsula. *Palaeogeogr. Palaeoclimatol. Palaeoecol.* **408**, 26–47 (2014).
60. Utescher, T. et al. The coexistence approach—theoretical background and practical considerations of using plant fossils for climate quantification. *Palaeogeogr. Palaeoclimatol. Palaeoecol.* **410**, 58–73 (2014).

61. Ballantyne, A. P. et al. Significantly warmer Arctic surface temperatures during the Pliocene indicated by multiple independent proxies. *Geology* **38**, 603–606 (2010).
62. Uhl, D., Mosbrugger, V., Bruch, A. & Utescher, T. Reconstructing palaeotemperatures using leaf floras—case studies for a comparison of leaf margin analysis and the coexistence approach. *Rev. Palaeobot. Palynol.* **126**, 49–64 (2003).
63. Pound, M. J. & Salzmann, U. Heterogeneity in global vegetation and terrestrial climate change during the late Eocene to early Oligocene transition. *Sci. Rep.* **7**, 43386 (2017).
64. Pross, J. et al. Persistent near-tropical warmth on the Antarctic continent during the early Eocene epoch. *Nature* **488**, 73–77 (2012).
65. Willard, D. A. et al. Arctic vegetation, temperature, and hydrology during Early Eocene transient global warming events. *Glob. Planet. Change* **178**, 139–152 (2019).
66. Kennedy, E. M. Late Cretaceous and Paleocene terrestrial climates of New Zealand: leaf fossil evidence from South Island assemblages. *N. Z. J. Geol. Geophys.* **46**, 295–306 (2003).
67. Kennedy, E. M. et al. Deriving temperature estimates from southern hemisphere leaves. *Palaeogeogr. Palaeoclimatol. Palaeoecol.* **412**, 80–90 (2014).
68. Grimm, G. W., Bouchal, J. M., Denk, T. & Potts, A. Fables and foibles: a critical analysis of the Palaeoflora database and the coexistence approach for palaeoclimate reconstruction. *Rev. Palaeobot. Palynol.* **233**, 216–235 (2016).
69. Hollis, C. J. et al. The DeepMIP contribution to PMIP4: methodologies for selection, compilation and analysis of latest Paleocene and early Eocene climate proxy data, incorporating version 0.1 of the DeepMIP database. *Geosci. Model Dev.* **12**, 3149–3206 (2019).
70. Kuhl, N., Gebhardt, C., Litt, T. & Hense, A. Probability density functions as botanical-climatological transfer functions for climate reconstruction. *Quat. Res.* **58**, 381–392 (2002).
71. Greenwood, D. R., Keefe, R. L., Reichgelt, T. & Webb, J. A. Eocene paleobotanical altimetry of Victoria’s Eastern Uplands. *Aust. J. Earth Sci.* **64**, 625–637 (2017).
72. *What is GBIF?* (GBIF, 2019); <https://www.gbif.org/what-is-gbif>
73. Fick, S. E. & Hijmans, R. J. WorldClim 2: new 1-km spatial resolution climate surfaces for global land areas. *Int. J. Climatol.* **37**, 4302–4315 (2017).
74. Hijmans, R. J., Phillips, S., Leathwick, J. & Elith, J. *dismo: Species Distribution Modeling R package version 1.1-4* (2017); <http://cran.r-project.org/web/packages/dismo/index.html>
75. Reichgelt, T., West, C. K. & Greenwood, D. R. The relation between global palm distribution and climate. *Sci. Rep.* **8**, 4721 (2018).
76. Bourbonniere, R. A. & Meyers, P. A. Sedimentary geolipid records of historical changes in the watersheds and productivities of Lakes Ontario and Erie. *Limnol. Oceanogr.* **41**, 352–359 (1996).
77. Rütters, H., Sass, H., Cypionka, H. & Rullkötter, J. Phospholipid analysis as a tool to study complex microbial communities in marine sediments. *J. Microbiol. Methods* **48**, 149–160 (2002).
78. Bauersachs, T., Talbot, H. M., Sidgwick, F., Sivonen, K. & Schwark, L. Lipid biomarker signatures as tracers for harmful cyanobacterial blooms in the Baltic Sea. *PLoS ONE* **12**, (2017).
79. Bauersachs, T. et al. Rapid analysis of long-chain glycolipids in heterocystous cyanobacteria using high-performance liquid chromatography coupled to electrospray ionization tandem mass spectrometry. *Rapid Commun. Mass Spectrom.* **23**, 1387–1394 (2009).
80. Bauersachs, T. et al. Distribution of long chain heterocyst glycolipids in cultures of the thermophilic cyanobacterium *Mastigocladus laminosus* and a hot spring microbial mat. *Org. Geochem.* **56**, 19–24 (2013).
81. Wörmer, L. et al. Cyanobacterial heterocyst glycolipids in cultures and environmental samples: diversity and biomarker potential. *Limnol. Oceanogr.* **57**, 1775–1788 (2012).
82. Schouten, S. et al. Endosymbiotic heterocystous cyanobacteria synthesize different heterocyst glycolipids than free-living heterocyst cyanobacteria. *Phytochemistry* **85**, 115–121 (2013).
83. Bale, N. J. et al. A novel heterocyst glycolipid detected in a pelagic N_2 -fixing cyanobacterium of the genus *Calothrix*. *Org. Geochem.* **123**, 44–47 (2018).
84. Bauersachs, T. et al. Heterocyst glycolipids indicate polyphyly of stigonematalean cyanobacteria. *Phytochemistry* **166**, (2019).
85. Ehrmann, W. et al. Provenance changes between recent and glacial-time sediments in the Amundsen Sea Embayment, West Antarctica: clay mineral assemblage evidence. *Antarct. Sci.* **23**, 471–486 (2011).
86. Petschick, R., Kuhn, G. & Gingele, F. Clay mineral distribution in surface sediments of the South Atlantic: sources, transport, and relation to oceanography. *Mar. Geol.* **130**, 203–229 (1996).
87. Kirschvink, J. L. The least-squares line and plane and the analysis of paleomagnetic data. *Geophys. J. Int.* **62**, 699–718 (1980).
88. Roeckner, E. et al. (eds) *PART I: Model Description Report No. 349* (Max-Planck-Institut für Meteorologie, 2003); http://www.mpimet.mpg.de/fileadmin/models/echam/mpir_report_349.pdf
89. Marsland, S. J., Haak, H., Jungclaus, J. H., Latif, M. & Roske, F. The Max-Planck-Institute global ocean/sea ice model with orthogonal curvilinear coordinates. *Ocean Model.* **5**, 91–127 (2003).
90. Hagemann, S. & Dumenil, L. A parametrization of the lateral waterflow for the global scale. *Clim. Dynam.* **14**, 17–31 (1997).
91. Hibler, W. D., III. A dynamic thermodynamic sea ice model. *J. Phys. Oceanogr.* **9**, 815–846 (1979).
92. Markwick, P. J. & Valdes, P. J. Palaeo-digital elevation models for use as boundary conditions in coupled ocean–atmosphere GCM experiments: a Maastrichtian (late Cretaceous) example. *Palaeogeogr. Palaeoclimatol. Palaeoecol.* **213**, 37–63 (2004).
93. Sewall, J. O. et al. Climate model boundary conditions for four Cretaceous time slices. *Clim. Past* **3**, 647–657 (2007).
94. Niezgodzki, I., Tyszka, J., Knorr, G. & Lohmann, G. Was the Arctic Ocean ice free during the latest Cretaceous? The role of CO_2 and gateway configurations. *Glob. Planet. Change* **177**, 201–212 (2019).

95. Wei, W. & Lohmann, G. Simulated Atlantic Multidecadal Oscillation during the Holocene. *J. Clim.* **25**, 6989–7002 (2012).
96. Zhang, X., Lohmann, G., Knorr, G. & Purcell, C. Abrupt glacial climate shifts controlled by ice sheet changes. *Nature* **512**, 290–294 (2014).
97. Stepanek, C. & Lohmann, G. Modelling mid-Pliocene climate with COSMOS. *Geosci. Model Dev.* **5**, 1221–1243 (2012).
98. Knorr, G. & Lohmann, G. Climate warming during Antarctic ice sheet expansion at the Middle Miocene transition. *Nat. Geosci.* **7**, 376–381 (2014).
99. Stein, R. et al. Evidence for ice-free summers in the late Miocene central Arctic Ocean. *Nat. Commun.* **7**, 11148 (2016).
100. Walliser, E. O., Lohmann, G., Niezgodzki, I., Tütken, T. & Schöne, B. R. Response of Central European SST to atmospheric $p\text{CO}_2$ forcing during the Oligocene—a combined proxy data and numerical climate model approach. *Palaeogeogr. Palaeoclimatol. Palaeoecol.* **459**, 552–569 (2016).
101. Vahlenkamp, M. et al. Astronomically paced changes in deep-water circulation in the Western North Atlantic during the Middle Eocene. *Earth Planet. Sci. Lett.* **484**, 329–340 (2018).
102. Gierz, P., Lohmann, G. & Wei, W. Response of Atlantic Overturning to future warming in a coupled atmosphere–ocean–ice sheet model. *Geophys. Res. Lett.* **42**, 6811–6818 (2015).
103. Simões Pereira, P. et al. Geochemical fingerprints of glacially eroded bedrock from West Antarctica: detrital thermochronology, radiogenic isotope systematics and trace element geochemistry in Late Holocene glacial-marine sediments. *Earth Sci. Rev.* **182**, 204–232 (2018).
104. Stacey, J. S. & Kramers, J. D. Approximation of terrestrial lead isotope evolution by a two-stage model. *Earth Planet. Sci. Lett.* **26**, 207–221 (1975).
105. Chew, D. M., Sylvester, P. J. & Tubrett, M. N. U–Pb and Th–Pb dating of apatite by LA-ICPMS. *Chem. Geol.* **280**, 200–216 (2011).
106. O’Sullivan, G. J., Chew, D. M., Morton, A. C., Mark, C. & Henrichs, I. A. An integrated apatite geochronology and geochemistry tool for sedimentary provenance analysis. *Geochem. Geophys. Geosyst.* **19**, 1309–1326 (2018).
107. Flowerdew, M. J. et al. Distinguishing East and West Antarctic sediment sources using the Pb isotope composition of detrital K-feldspar. *Chem. Geol.* **292–293**, 88–102 (2012).
108. Petrus, J. A. & Kamber, B. S. VizualAge: a novel approach to laser ablation ICP-MS U–Pb geochronology data reduction. *Geostand. Geoanal. Res.* **36**, 247–270 (2012).
109. Chew, D. M., Petrus, J. A. & Kamber, B. S. U–Pb LA-ICPMS dating using accessory mineral standards with variable common Pb. *Chem. Geol.* **363**, 185–199 (2014).
110. Paton, C., Hellstrom, J., Paul, B., Woodhead, J. & Hergt, J. Lolite: freeware for the visualisation and processing of mass spectrometric data. *J. Anal. Atom. Spectrom.* **26**, 2508–2518 (2011).
111. Ludwig, K. R. *User’s Manual for Isoplot 3.75: A Geochronological Toolkit for Microsoft Excel* Special Publication No. 4 (Berkeley Geochronology Center, 2012).
112. Nasdala, L. et al. GZ7 and GZ8—two zircon reference materials for SIMS U–Pb geochronology. *Geostand. Geoanal. Res.* **42**, 431–457 (2018).
113. McDowell, F. W., McIntosh, W. C. & Farley, K. A. A precise ^{40}Ar – ^{39}Ar reference age for the Durango apatite (U–Th)/He and fission-track dating standard. *Chem. Geol.* **214**, 249–263 (2005).
114. Schoene, B. & Bowring, S. A. U–Pb systematics of the McClure Mountain syenite: thermochronological constraints on the age of the ^{40}Ar – ^{39}Ar standard MMhb. *Contrib. Mineral. Petrol.* **151**, 615 (2006).
115. Mark, C., Cogné, N. & Chew, D. Tracking exhumation and drainage divide migration of the western Alps: a test of the apatite U–Pb thermochronometer as a detrital provenance tool. *Geol. Soc. Am. Bull.* **128**, 1439–1460 (2016).
116. Mao, M., Rukhlov, A. S., Rowins, S. M., Spence, J. & Coogan, L. A. Apatite trace element compositions: a robust new tool for mineral exploration. *Econ. Geol.* **111**, 1187–1222 (2016).
117. Woodhead, J. D., Hellstrom, J., Hergt, J. M., Greig, A. & Maas, R. Isotopic and elemental imaging of geological materials by laser ablation inductively coupled plasma-mass spectrometry. *Geostand. Geoanal. Res.* **31**, 331–343 (2007).

Acknowledgements We thank the captain and crew of RV *Polarstern* Expedition PS104, as well as the MARUM-MeBo70 team for their support; S. Wiebe, R. Fröhlking-Teichert, V. Schumacher, N. Lensch, M. Arevalo, M. Seebeck and H. Grobe for their help on board and in the lab, respectively; the Klinikum Bremen-Mitte (A.-J. Lemke and C. Tiemann, Gesundheit Nord Bremen) for providing facilities for computed core tomographies and M. Köhler (MKfactory, Stahnsdorf, Germany) for preparing the thin sections; and J. McKay (University of Leeds, UK) for creating and painting the Late Cretaceous West Antarctic palaeoenvironment based on reconstructions presented here. The operation of MARUM-MeBo70 was funded by the Alfred Wegener Institute (AWI) through its Research Program PACES II Topic 3 and grant no. AWI_PS104_001, the MARUM Center for Marine Environmental Sciences, the British Antarctic Survey through its Polar Science for Planet Earth programme and the Natural Environmental Research Council-funded UK IODP programme. J.P.K., G.K., K.G., J.M. G.U.-N., O.E., C.G., T.R. and R.D. were funded by the AWI PACES II programme. J.P.K. and J.M. were also funded through the Helmholtz Association (PD-201 and VH-NG-1101). UK IODP funded the participation of T.v.d.F., P.S.P. and S.M.B. in expedition PS104. J.T. was funded through the Cluster of Excellence “The Ocean Floor – Earth’s Uncharted Interface” at the University of Bremen. Y.N. was funded by Lancaster University, UK.

Author contributions J.P.K. led the study and together with U.S., T. Bickert, C.-D.H., K.G. and G.K., conceived the idea for the study and wrote the manuscript. J.P.K., T. Bickert, C.-D.H., S.M.B., J.A.S., K.G., T. Freudenthal, T.v.d.F., P.S.P., W.E., O.E., H.P. and T.R. collected the cores. J.P.K., C.-D.H., T. Bickert and G.K. undertook the sedimentological and U.S. and S.M.B. the palynological analyses. T. Bickert and G.K. conducted the XRF scanning and processing of the cores. G.K. carried out the grain-size and bulk mineralogical analyses. J.T. led the CT scanning, processing and visualization. J.M. performed the biomarker analyses (apolar hydrocarbons) together with T. Bauersachs (HG palaeothermometry). T. Frederichs conducted the palaeomagnetic measurements. J.E.F., G.N., G.K. and J.P.K. investigated the thin sections. W.E. analysed the clay mineral assemblages and T.v.d.F. and P.S.P. measured bulk sediment Nd and Sr isotope compositions. K.G., R.D.L. and T. Frederichs helped determine the palaeolatitudes of the drill site. G.L. and I.N. undertook the modelling with COSMOS. M.Z., C.S., C.M. and D.C. provided the U–Pb age constraints. U.S. and F.S. performed the bioclimatic analyses. J.P.K., T.B., C.-D.H., S.M.B., T. Frederichs, W.E., J.A.S., O.E., H.P., T.R. and R.D. helped with sampling and scanning the cores. K.G., G.U.-N. and R.D.L. undertook the seismic pre-site survey. All members of the Expedition PS104 Science Team helped with pre-site survey investigations, core recovery, onboard analyses and/or shore-based measurements. K.G., G.K., C.-D.H., G.U.-N., T. Bickert and R.D.L. acquired funding and proposed and planned RV *Polarstern* expedition PS104. All co-authors commented on the manuscript and provided input to its final version.

Competing interests The authors declare no competing interests.

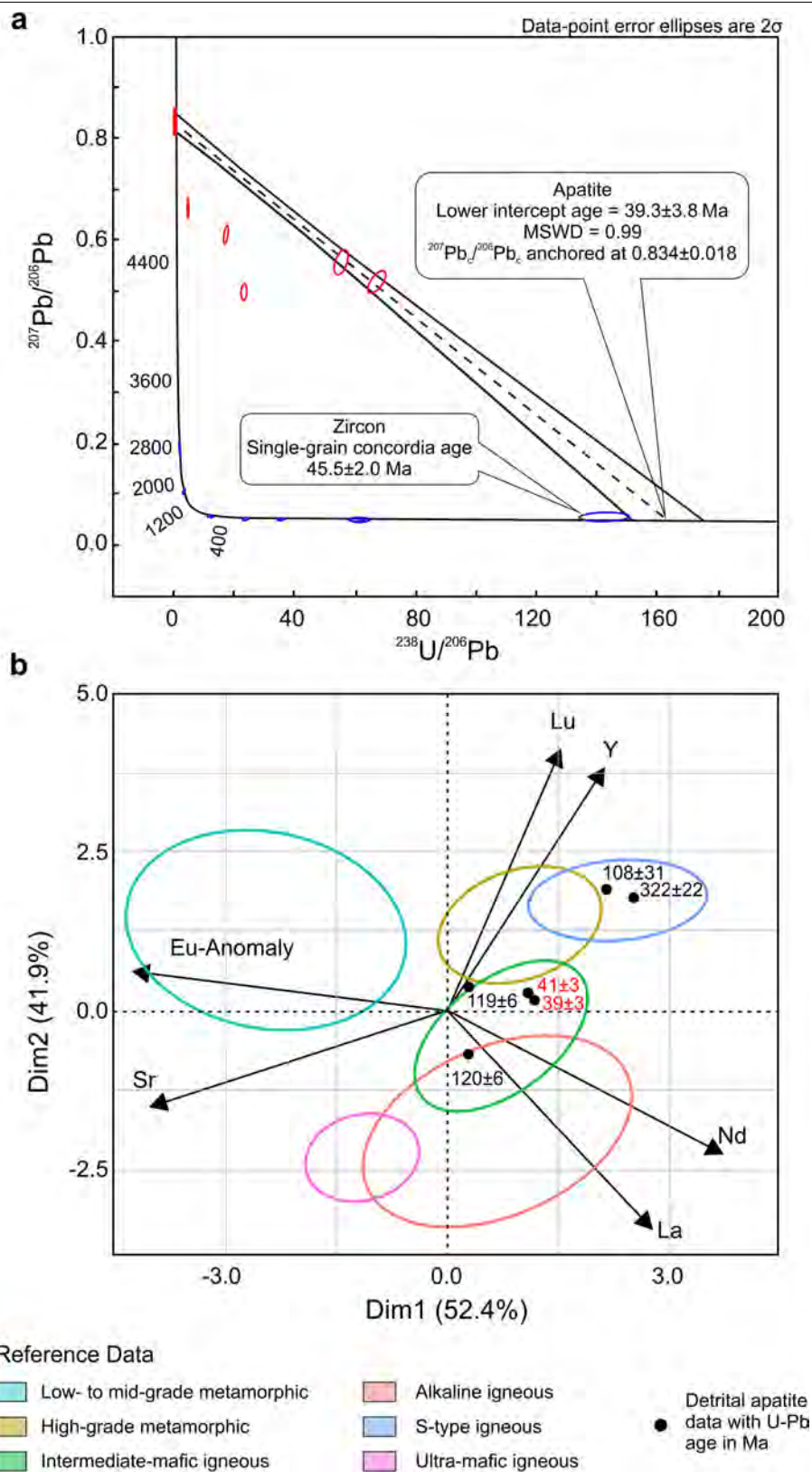
Additional information

Supplementary information is available for this paper at <https://doi.org/10.1038/s41586-020-2148-5>.

Correspondence and requests for materials should be addressed to J.P.K.

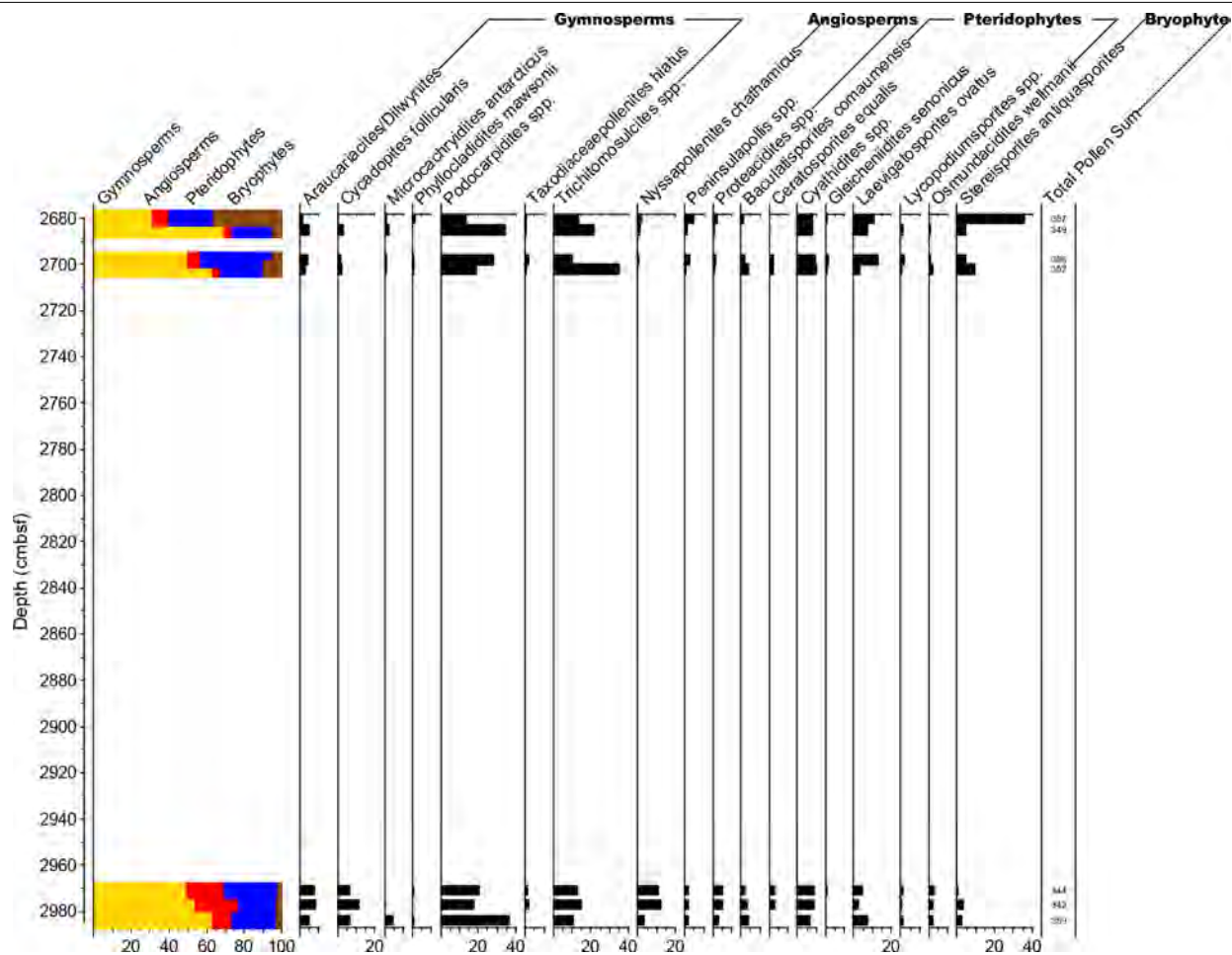
Peer review information *Nature* thanks Dietmar Muller, Anne-Marie Tosolini and the other, anonymous, reviewer(s) for their contribution to the peer review of this work.

Reprints and permissions information is available at <http://www.nature.com/reprints>.

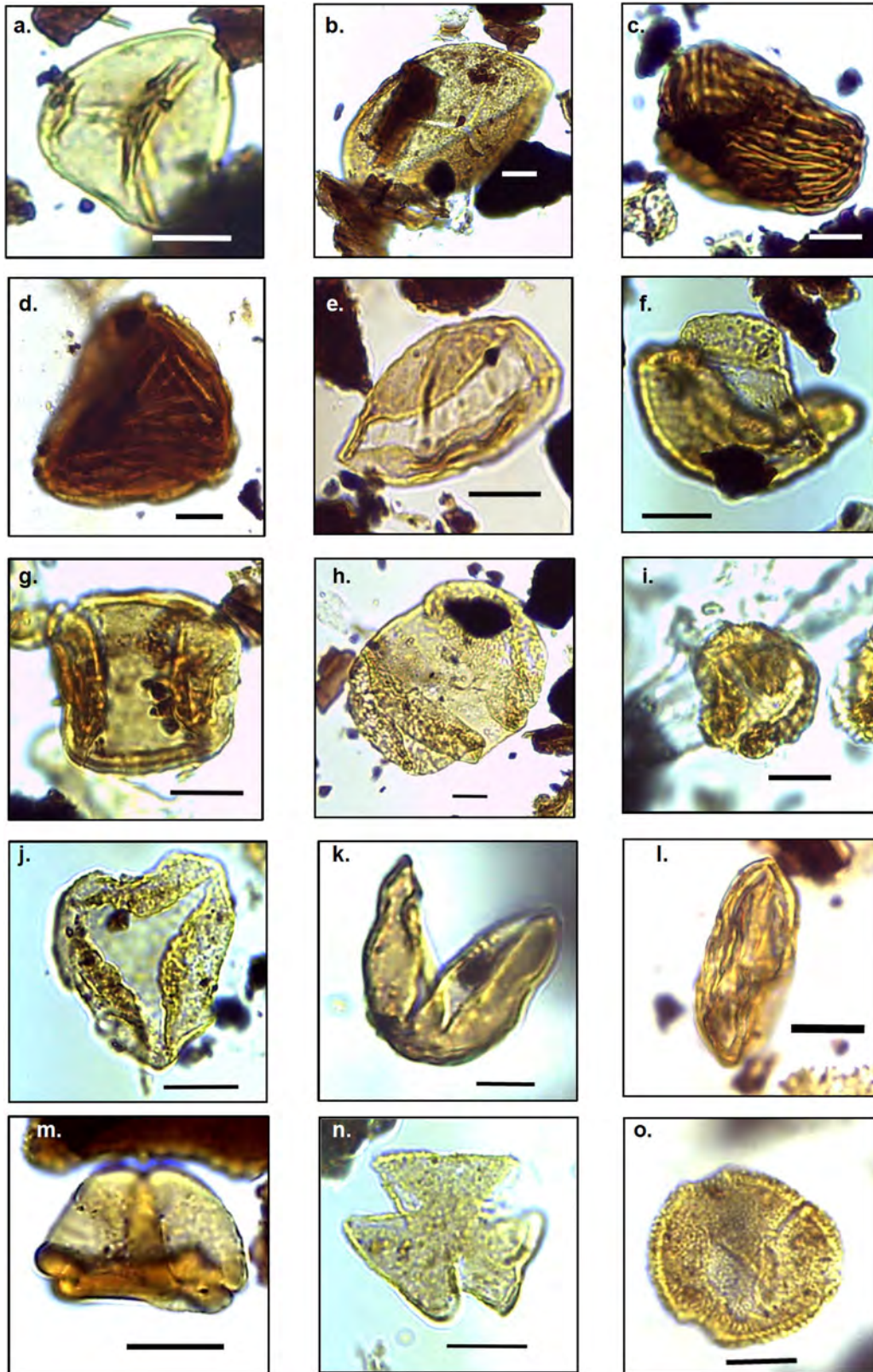


Extended Data Fig. 1 | Tera-Wasserburg and PCA plots for U-Pb ages (in \pm Ma). **a**, Tera-Wasserburg diagram showing apatite (red; 9.9 mbsf) and zircon (blue; 26.7 mbsf) U-Pb data. The red bar at the upper array intercept for Eocene apatite is the range of crystalline basement $^{207}\text{Pb}/^{206}\text{Pb}_c$ values reported by (ref. ¹⁰⁴) for West Antarctica, which anchor the apatite age

calculation. **b**, PCA plot showing trace-element data and single-grain ages (in Myr) for AWI-35 (9.9 mbsf) apatite, and lithological fields derived from a bedrock apatite reference library¹⁰⁴. Eocene grains (labelled in red) are chemically and chronologically distinct from other detrital apatite in the same sample. Data point error ellipses are 2σ .



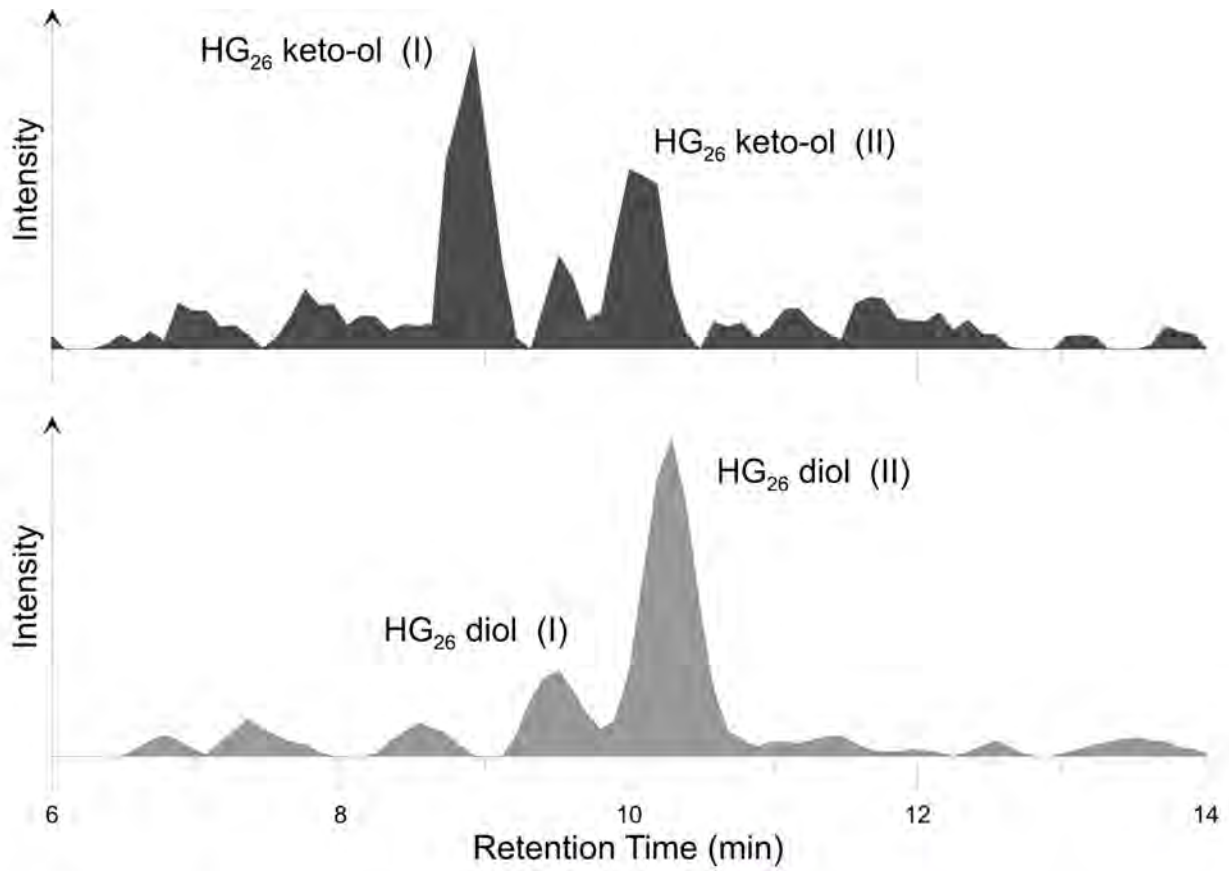
Extended Data Fig. 2 | Pollen abundance diagram. Percentages of the most abundant pollen and spores and their total counts in cores 9R and 10R at site PS104_20-2 are shown.



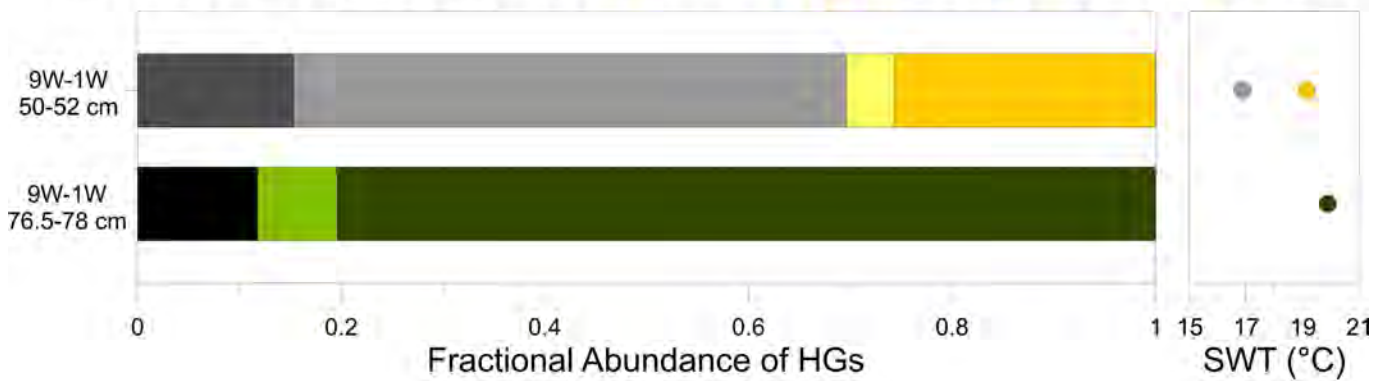
Extended Data Fig. 3 | Photomicrographs of selected pollen and spores.

a, *Cyathidites australis*. **b**, *Osmundacidites wellmanii*. **c**, *Ruffordiaspora australiensis*. **d**, *Ruffordiaspora ludbrookiae*. **e**, *Cycadopites follicularis*. **f**, *Microcachrydites antarcticus*. **g**, *Phyllocladidites mawsonii*. **h**, *Podocarpidites*

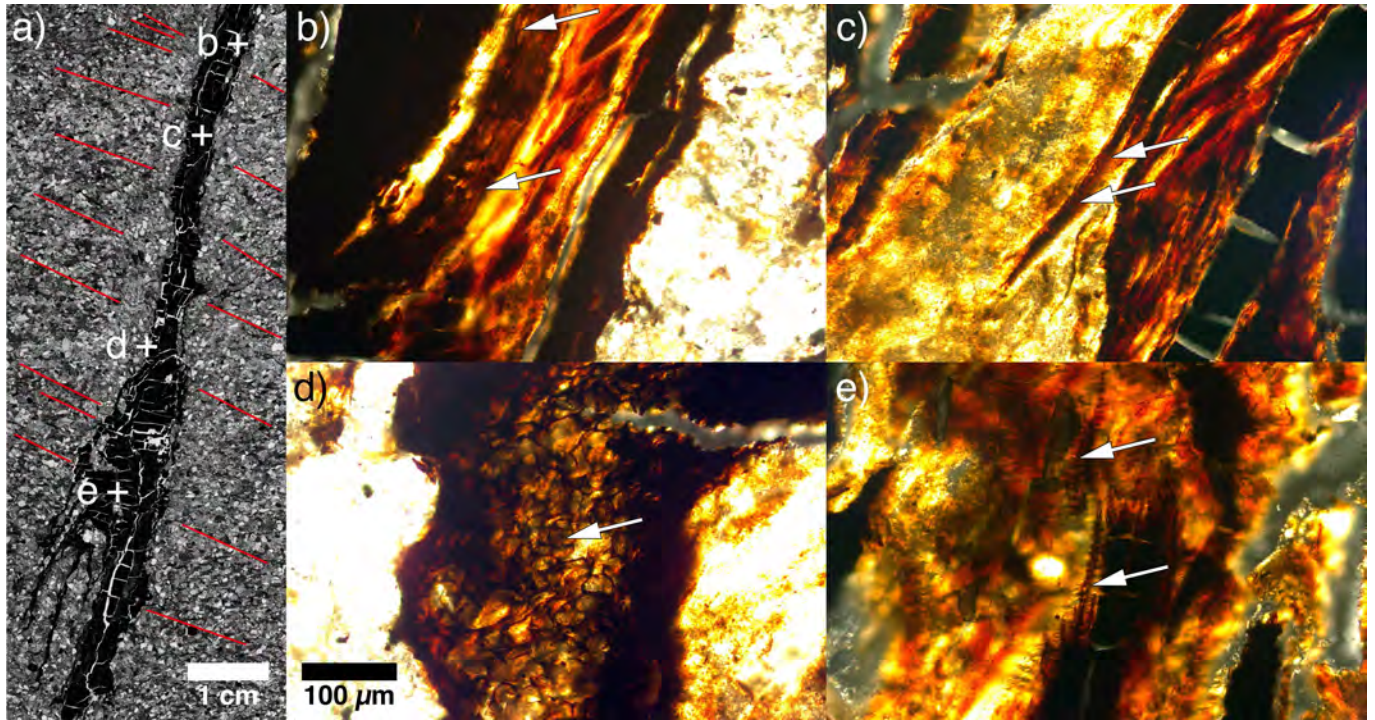
major. **i**, *Trichotomosulcites hemisphaerius*. **j**, *Trichotomosulcites subgranulatus*. **k**, *Taxodiaceapollenites hiatus*. **l**, *Equisetosporites* sp. **m**, *Nyssapollenites chathamicus*. **n**, *Peninsulapollis gillii*. **o**, *Proteacidites subpalisadus*. Scale bars, 10 μ m.



P HG₂₆ diol
 HG₂₆ keto-ol
 HG₂₆ diol
 HG₂₈ keto-ol
 HG₂₈ diol
 HG₃₀ keto-diol
 HG₃₀ triol

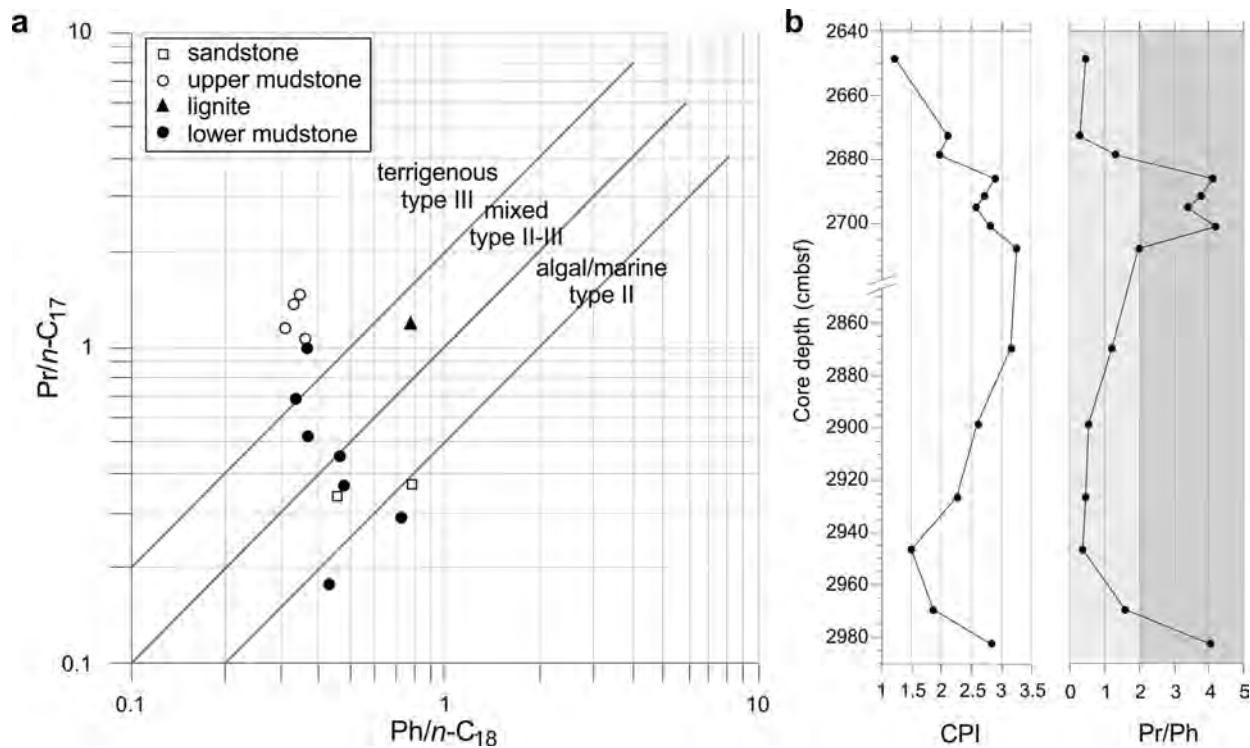


Extended Data Fig. 4 | HG palaeothermometry. Presence of HGs at 27.03–27.04 mbsf at site PS104_20-2 (core 9R) and river or lake surface water temperature (SWT) estimates from the HG-based molecular palaeothermometer (HTI₃₀).



Extended Data Fig. 5 | Example microscopic images from thin sections. The sections are taken from a fossil root fragment between 29.34 and 29.43 mbsf in core 10R at site PS104_20-2. **a**, Overview scan of root fragment with indicated

locations of detailed microscopic images **b–e**. White arrows indicate the locations of preserved parenchyma storage cells, including potential aerenchyma gas exchange cells (**d**). The scale bar in **d** applies to **b–e**.



Extended Data Fig. 6 | Biomarker presence. a, Pristane/ n -C₁₇ versus phytane/ n -C₁₈ to infer organic matter type during sediment deposition (after refs.^{37,38}). **b,** CPI (left) and pristane/phytane (Pr/Ph; right) ratios. The CPI points

to a low maturity and land plant origin of the organic matter (CPI > 1) deposited in an aquatic environment (Pr/Ph < 2) and a peat swamp environment (Pr/Ph > 2), respectively.

Article

Extended Data Table 1 | Percentages of the most abundant pollen and spore taxa

Depth (cmbsf)	2680	2685	2698	2702	2971	2977	2984
Core	020--2	020--2	020--2	020--2	020--2	020--2	020--2
Section	9R-1W	9R-1W	9R-1W	9R-1W	10R-1W	10R-1W	10R-1W
Core depth (cm)	55	60	73	77	111	117	172
Gymnosperms	31.4	69.1	49.6	63.1	49.1	54.4	63.2
Angiosperms	8.7	4.3	7.4	4.3	20.6	22.5	10.3
Pteridophytes	23.8	21.7	37.9	23	27.9	20.2	23.7
Bryophytes	36.1	4.9	5.1	9.7	2.4	2.9	2.8
<i>Araucariacites/Dilwynites</i>	1.1	4.9	4.2	2.8	7.3	8.2	4.7
<i>Cycadopites follicularis</i>	0.3	2.9	1.7	2.6	6.4	11.4	6.4
<i>Microcachrydites antarcticus</i>	0.8	2.3	1.1	0.9	0	0.6	4.2
<i>Phyllocladidites mawsonii</i>	1.1	0	0.6	0.9	0.6	0	0.6
<i>Podocarpidites spp.</i>	13.7	34.1	28.1	19.3	20.3	17.8	36.5
<i>Taxodiaceapollenites hiatus</i>	0.8	0.6	2.2	0.6	1.2	1.8	0
<i>Trichitomosulcites spp.</i>	13.4	21.5	9.8	35.2	12.8	14.6	10.9
<i>Nyssapollenites chathamicus</i>	1.7	1.1	0.3	0	11	12	3.3
<i>Peninsulapollis spp.</i>	4.5	1.1	2.5	0.6	2	1.8	1.9
<i>Proteacidites spp.</i>	2.5	0.9	1.4	1.1	5.2	5	2.8
<i>Baculatisporites comaumensis</i>	1.1	0	2	4	2	2.9	3.9
<i>Ceratospores equalis</i>	0	0.3	2	2	3.2	2.9	0.3
<i>Cyathidites spp.</i>	8.4	8.3	9.8	9.9	8.7	8.8	7
<i>Gleicheniidites senonicus</i>	0.8	0.3	1.7	0.6	0.9	0	0
<i>Laevigatosporites ovatus</i>	10.6	7.4	12.9	2.8	4.4	2.6	7.2
<i>Lycopodiumsporites spp.</i>	0	0.9	1.7	0.3	1.2	0.3	1.4
<i>Osmundacidites wellmanii</i>	0.3	0.6	0.8	2.3	2.6	2	2.5
<i>Stereisporites antiquasporites</i>	36.1	4.9	4.5	9.4	0.6	2.9	2.2
Total Pollen Sum	357	349	356	352	344	342	359
Pollen concentration (grains/g)	69320	55144	61895	121476	4250	6900	7869

Extended Data Table 2 | Key pollen taxa and the NLRs used to derive quantitative climate estimates

Selected Pollen Taxa	Botanical Affinity (after Raine et al. 2011)	Selected NLRs for Bioclimatic Analysis
Gymnosperms		
<i>Araucariacites/Dilwynites</i>	Araucariaceae (<i>Araucaria</i> , <i>Agathis</i>)	<i>Araucaria</i>
<i>Cycadopites follicularis</i>	Gymnospermopsida	<i>Cycadales</i>
<i>Equisetosporites</i>	Ephedraceae (<i>Ephedra</i> , cf. <i>E. chinleana</i>)	<i>Ephedra</i>
<i>Microcachrydites antarcticus</i>	Podocarpaceae (<i>Microstrobos</i> , <i>Microcachrys tetragona</i>)	<i>Podocarpus</i>
<i>Phyllocladites mawsonii</i>	Podocarpaceae (aff. <i>Lagarostrobos franklinii</i>)	<i>Lagarostrobos</i>
<i>Podocarpidites ellipticus</i> ; <i>P. major</i>	Podocarpaceae (<i>Podocarpus</i> ?)	<i>Podocarpus</i>
<i>Podocarpidites otagoensis</i>	Podocarpaceae (<i>Podocarpus</i> ?, or <i>Lagarostrobos</i>)	<i>Podocarpus</i>
<i>Taxodiaceapollenites hiatus</i>	Cupressaceae, Taxodiaceae	Cupressaceae
<i>Trichotomosulcites subgranulatus</i>	Podocarpaceae. Extinct <i>Microcachrys</i>	Podocarpaceae
Angiosperms		
<i>Liliacidites cf. variegatus</i>	Liliaceae; Monimiaceae (cf. <i>Laurelia novaezealandiae</i>)	Liliaceae
<i>Peninsulapollis gillii</i> ; <i>P. truswellia</i>	Proteaceae	Proteaceae
<i>Proteacidites parvus</i>	Proteaceae (<i>Bellendena montana</i> type)	Proteaceae
<i>Proteacidites minimus</i>	Proteaceae (<i>Knightia excelsa</i>)	Proteaceae
Pteridophytes		
<i>Baculatisporites comaumensis</i>	Osmundaceae (<i>Osmunda</i> , <i>Leptopteris</i>); Hymenophyllaceae (<i>Hymenophyllum flexuosum</i> , <i>H. cruentum</i>)	Hymenophyllaceae
<i>Ceratospores equalis</i>	Lycopodiaceae, Selaginellaceae (<i>Selaginella</i> , e.g. <i>S. tenuispinulosa</i>)	Selaginellaceae
<i>Cibotiidites tuberculiformis</i>	Dicksoniaceae (cf. <i>Dicksonia squarrosa</i> , <i>D. dissecta</i>); Schizaeaceae	Dicksoniaceae
<i>Cyathidites australis</i> ; <i>C. minor</i>	Cyatheaceae (<i>Cyathea</i>), Dicksoniaceae, Schizaeaceae (<i>Lygodium</i>)	Cyatheaceae
<i>Gleicheniidites senonicus</i>	Gleicheniaceae (<i>Gleichenia circinata</i> group, <i>Dicranopteris</i>)	Gleicheniaceae
<i>Laevigatosporites ovatus</i>	Aspleniaceae, Blechnaceae, Polypodiaceae, Schizaeaceae	Polypodiaceae
<i>Lycopodiumsporites sp.</i>	Lycopodiaceae (<i>Lycopodium</i>)	Lycopodiaceae
<i>Osmundacidites wellmanii</i>	Osmundaceae (<i>Todea barbara</i>)	Osmundaceae
<i>Perotrilites majus</i>	Selaginellaceae?	Selaginellaceae
<i>Polypodiisporites cf. minimus</i>	Davalliaceae (<i>Nephrolepis</i>)	Davalliaceae
<i>Ruffordiaspora australiensis</i>	Schizaeaceae	Schizaeaceae
Bryophytes		
<i>Stereisporites antiquasporites</i>	Bryophyta; <i>Sphagnum</i>	<i>Sphagnum</i>

Article

Extended Data Table 3 | Full list of identified pollen and spore taxa

Bryophytes

**Aequitriradites spinulosus* (Cookson & Dettmann)
**Annulispora folliculosa* (Rogalska)
**Coptospora striata* (Dettmann)
**Foraminisporis cf. F. wonthaggiensis* (Cookson & Dettmann)
**Stereisporites antiquasporites* (Dettmann)

Pteridophytes

**Baculatisporites comaumensis* (Cookson)
**Biretisporites* sp.
**Ceratospores equals* (Cookson & Dettmann)
Cibotidites tuberculiformis (Cookson)
**Crybelosporites striatus* (Cookson & Dettmann)
**Cyathidites cf. C. asper* (Bolkhovitina)
**Cyathidites minor* (Couper)
**Cyathidites cf. C. punctatus* (Delcourt & Sprumont)
**Cyathidites* undiff.
**Gleicheniidites senonicus* (Ross)
Herkosporites sp.
**Laevigatosporites ovatus* (Wilson & Webster)
Lycopodiadites cf. L. dettmannae (Burger)
**Lycopodiumsporites* sp.
**Osmundadites wellmanii* (Couper)
Polypodiisporites sp.
**Perotriletes cf. P. majus* (Cookson & Dettmann)
**Reticulatisporites cf. R. pudens* (Balme)
**Retriletes austroclavatidites* (Cookson)
Retriletes cf. R. rosewoodensi (de Jersey)
**Retriletes* undiff.
**Ruffordiaspora australiensis* (Cookson)
**Ruffordiaspora ludbrookiae* (Dettmann)

Gymnosperms

**Araucariacites/Dilwynites*
**Callialasporites dampieri* (Balme)
**Classopollis cf. chateaunovi* (Reyre)
**Cycadopites follicularis* (Wilson & Webster)
**Dacrydiumites praecupressinoides* (Couper)
**Equisetosporites* sp.
**Microcachrydites antarcticus* (Cookson)
**Phyllocladidites mawsonii* (Cookson)
**Podocarpidites cf. P. ellipticus* (Cookson)
**Podocarpidites cf. P. major* (Couper)
**Podocarpidites cf. P. otagoensis* (Couper)
**Podocarpidites* undiff.
**Podosporites* sp.
**Taxodiaceapollenites hiatus* (Potonie)
**Trichotomosulcites hemisphaerius* (Mays)
**Trichotomosulcites subgranulatus* (Couper)
**Triletes* undiff.

Angiosperms

?*Beaupreoidites verrucosus* (Cookson)
**Cupuliferoidapollenites cf. C. parvulus* (Groot & Penny)
**Liadidites cf. L. intermedius* (Couper)
**Monosulcites* undiff.
**Nyssapollenites chathamicus* (Mildenhall)
Peninsulapollis gillii (Cookson)
Peninsulapollis truswellii (Dettmann & Jarzen)
**Phimopollenites augathalaensis*
**Polycopropollenites esobalteus*
Proteacidites parvus (Cookson)
Proteacidites cf. P. subpalisadus (Couper)
Proteacidites cf. P. subscabratus (Couper)
Proteacidites minimus (Couper)
Proteacidites sp.
**Rousea georgensis* (Brenner)
**Tetracolpites* sp.
**Tricolpites cf. T. pachyaxinus* (Couper)
**Tricolpites minutus* (Brenner)
**Tricolpites* sp.
Triorites sp.

All taxa identified during the current study are included. Question marks show uncertain taxon identifications that require further study. *Taxa described from the Tupuangi Formation on the Chatham Islands^{28,58}.